AD-A133 669 INFLUENCE OF RARE-EARTH ADDITIONS ON PROPERTIES OF TITANIUM ALLOYS EFFECT..(U) MCDONNELL DOUGLAS RESEARCH LABS ST LOUIS MO S M SASTRY ET AL. 31 JUL 82 MDC-Q0791 1/1

UNCLASSIFIED N00014-76-C-0626 F/G 11/6 NL

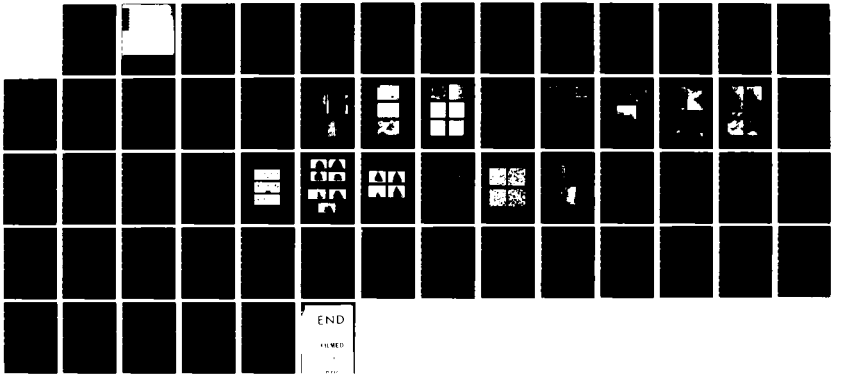

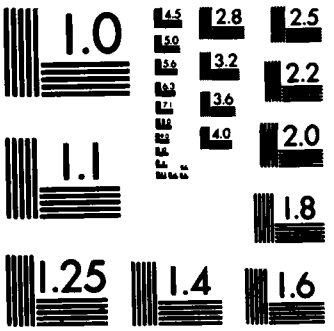

MICROCOPY RESOLUTION TEST CHART
NATIONAL BUREAU OF STANDARDS-1963-A

AD-A133 669

DTIC FILE COPY

MCDONNELL DOUGLAS RESEARCH LABORATORIES

MCDONNELL DOUGLAS CORPORATION

DISTRIBUTION STATEMENT A
Approved for public release;
Distribution Unlimited

83 10 13 006

Delete Dist. St on cover per Dr. Bruce MacDonald, ORR
M. Cumbackee
18 Oct 83

UNCLASSIFIED

SECURITY CLASSIFICATION OF THIS PAGE (When Data Entered)

REPORT DOCUMENTATION PAGE		READ INSTRUCTIONS BEFORE COMPLETING FORM
1. REPORT NUMBER MDC Q0791	2. GOVT ACCESSION NO. AD-A133669	3. RECIPIENT'S CATALOG NUMBER
4. TITLE (and Subtitle) INFLUENCE OF RARE-EARTH ADDITIONS ON PROPERTIES OF TITANIUM ALLOYS Effects of Yttrium and Erbium Additives on Rapid Solidification Processing, Superplastic Forming, Welding, and Strengthening of Titanium Alloys		5. TYPE OF REPORT & PERIOD COVERED Final Report 1 Sep 80 - 31 Jul 82 6. PERFORMING ORG. REPORT NUMBER
7. AUTHOR(s) S. M. L. Sastry, T. C. Peng, R. J. Lederich, J. E. O'Neal		8. CONTRACT OR GRANT NUMBER(s) N00014-76-C-0626
9. PERFORMING ORGANIZATION NAME AND ADDRESS McDonnell Douglas Research Laboratories McDonnell Douglas Corporation St. Louis, MO 63166		10. PROGRAM ELEMENT, PROJECT, TASK AREA & WORK UNIT NUMBERS
11. CONTROLLING OFFICE NAME AND ADDRESS Office of Naval Research 800 N. Quincy Street Arlington, VA 22217		12. REPORT DATE 31 July 1982 13. NUMBER OF PAGES
14. MONITORING AGENCY NAME & ADDRESS(if different from Controlling Office)		15. SECURITY CLASS. (of this report) Unclassified 15a. DECLASSIFICATION/DOWNGRADING SCHEDULE

16. DISTRIBUTION STATEMENT (of this Report)

Approved for public release; distribution unlimited.

17. DISTRIBUTION STATEMENT (of the abstract entered in Block 20, if different from Report)

18. SUPPLEMENTARY NOTES

greater than 10000

19. KEY WORDS (Continue on reverse side if necessary and identify by block number)

Titanium alloy	Yttrium	Solid solution strengthening
Ti-6Al-2Nb-1Mo-0.8Ta	Erbium	Grain size strengthening
Ti-6Al-4V	Rapid solidification	Dispersion strengthening
Ti-8Al	Superplastic formability	Microstructure
Ti-10Al	Welding	Grain refinement

20. ABSTRACT (Continue on reverse side if necessary and identify by block number)

Effects of 0.01-2.0 wt% yttrium and erbium additions on rapid solidification processing, superplastic forming, welding, and strengthening of titanium alloys were determined. Ti-8Al-Y and Ti-8Al-Er alloys were rapidly solidified by laser surface melting and electron beam melting and splat-quenching with the objective of simultaneously producing coherent Ti_3Al precipitates and incoherent dispersoids. Rapid solidification at cooling rates > 10^4 K/s resulted in 10-100 nm incoherent dispersoids in Ti-8Al-1.5Y and in a nonequilibrium, supersaturated, solid solution in Ti-8Al-1.5Si. Dispersoid formation and

DD FORM 1 JAN 73 1473 EDITION OF 1 NOV 65 IS OBSOLETE

UNCLASSIFIED

SECURITY CLASSIFICATION OF THIS PAGE (When Data Entered)

19. continued

Precipitation strengthening Ductility

20. continued

stability at 700-900°C were studied, and the annealing conditions for the production of a large volume-fraction of fine incoherent dispersoids and of coherent Ti_3Al precipitates were determined. Metallic yttrium additions to Ti-6Al-2Nb-1Mo-0.8Ta improved the superplastic formability and increased the strength and ductility of laser weldments. The superposition of solid-solution strengthening, precipitation strengthening, and grain-size strengthening in ingot processed Ti-xAl (x = 4, 5.5, 7.0, 8.5, and 10.0) alloys was studied. The Hall-Petch slope decreased with decreasing Al concentration, decreasing coherent Ti_3Al, and increasing incoherent dispersoids. Yttrium additions to ingot processed Ti-high Al alloys did not produce additional strengthening because of scavenging of interstitial oxygen by yttrium and large interparticle spacings. 0.2-1.0 wt% silicon additions to Ti-8.5Al resulted in 50-140 MPa strength increments because of grain refinement of Si and the increased Hall-Petch slope in silicon containing alloys.

PREFACE

This report represents the results of the final phase of an investigation of the effects of rare-earth additives on titanium alloys performed by the McDonnell Douglas Research Laboratories under Office of Naval Research Contract No. N00014-76-C-0626. The Scientific Officer for the contract was Dr. Bruce A. MacDonald of ONR.

The principal investigator was Dr. Shankar M. L. Sastry; coinvestigators were Mr. Richard J. Lederich and Mr. James E. O'Neal. The work was performed in the Solid State Science department under the direction of Dr. Charles R. Whitsett.

This report has been reviewed and is approved.

Charles R. Whitsett

Charles R. Whitsett
Director-Research
McDonnell Douglas Research Laboratories

D. P. Ames

D. P. Ames
Staff Vice President
McDonnell Douglas Research Laboratories

Accession For	
NTIS GRA&I	X
DTIC TAB	☐
Unannounced	☐
Justification	
By	
Distribution/	
Availability Codes	
Dist	Avail and/or Special
A	

DTIC COPY INSPECTED

Delete Dist. St. on cover per Dr. Bruce A. MacDonald, ONR
Dist. St. on DD 1473 is correct.

M. Crumbacker
DTIC-DDAC
18 Oct 83

TABLE OF CONTENTS

TABLE OF CONTENTS (continued)

LIST OF ILLUSTRATIONS

LIST OF ILLUSTRATIONS (continued)

LIST OF TABLES

1. INTRODUCTION

A systematic investigation of the effects of metallic rare-earth (RE) additions on the microstructures and properties of Ti alloys was conducted during preceding phases of this program (References 1-5). The primary objective of the preceding phases was to improve the high-temperature forgeability of Ti-6Al-4V by small amounts of rare-earth additions. The addition of 0.02-0.1 wt% Er or Y was shown to produce fine (< 0.1 μm) incoherent dispersoids, retard grain growth, and improve the forgeability, high-temperature formability, and ductility of Ti-6Al-4V without adversely affecting tensile strength and fracture toughness. The study was then extended to determine the feasibility of improving the ductility of precipitation-strengthened Ti-8Al and Ti-10Al alloys by fine, incoherent dispersoids and grain refinement produced by the rare-earth element additions.

Small rare-earth additions substantially increase the ductility without adversely affecting the strength of conventionally cast Ti-8Al and Ti-10Al alloys. The improved ductility at low levels of rare-earth concentrations results from the reduction of the interstitial concentration by the oxygen scavenging of Er and Y. Rare-earth additions in concentrations sufficiently large to produce significant dispersion strengthening precipitated as coarse particles and embrittled the alloys.

In the present phase, rapid solidification to produce large concentrations of fine rare-earth dispersoids for dispersion strengthening of Ti-Al alloys was investigated, and the effects of Y and Er additions on superplastic formability, weldability, and strengthening of Ti alloys were determined. The results of rapid solidification are presented in Section 2. The superplastic formability improvements produced by Y and Y_2O_3 additions to Ti-6Al-4V and Ti-6Al-2Nb-1Mo-0.8Ta are presented in Section 3. The effects of Y and Y_2O_3 additions on the weldability of Ti-6Al-2Nb-1Mo-0.8Ta are presented in Section 4, and the combined effects of solid solution, grain size, and dispersion strengthening in Ti-8Al and Ti-10Al alloys are presented in Section 5.

2. RAPID SOLIDIFICATION PROCESSING OF TITANIUM/RARE-EARTH ALLOYS

2.1 Rapid Solidification by Laser Surface Melting and Electron-Beam Melting and Splat Quenching

Laser surface melting was used to determine the effect of rapid solidification on dispersoid refinement. To obtain rapid solidification by laser processing, the surface of a material is irradiated with a laser beam focused to a power density of 10^5-10^7 W/cm^2 at traverse rates of 10-100 cm/s. A thin, molten layer formed by laser irradiation solidifies rapidly on the alloy substrate following passage of the laser beam. By varying the power density and traverse rate, melt depths of 10-100 μm and cooling rates of 10^3-10^6 °C/s can be produced. The technique of producing surface alloys by laser processing is attractive for studying the dependence of microstructures on alloying element concentration and cooling rate for a variety of alloy systems. Furthermore, laser processing is an inexpensive technique for screening large numbers of candidate compositions in the development of new alloys by rapid solidification processing (RSP). In the present investigation, several titanium alloys were surface-melted and surface-alloyed using a 1.5-kW, continuous-wave, CO_2 laser with the objectives of determining the interrelation between process parameters, melt-zone geometry, and microstructures and evaluating the feasibility of producing fine, 10-100 nm diameter, stable, incoherent dispersoids in rapidly solidified Ti alloys.

Ti-Y, Ti-8Al, Ti-8Al-0.5Y, Ti-8Al-1.0Y, and Ti-8Al-2.0Er alloys were used for laser melting and laser alloying. The starting alloys were prepared by nonconsumable-electrode arc-melting in pure argon, and 1.6-mm and 3.0-mm thick sheets were produced by unidirectional hot rolling. The surface coatings for laser surface-alloying studies were produced by electron-beam evaporation of the coating elements onto the Ti-alloy substrates in a vacuum of 10^{-4} Pa. Laser surface-melting and surface-alloying experiments were conducted on 25 x 30 x 1.6-mm specimens with 1.5-kW CO_2 laser using the experimental arrangement shown in Figure 1. The specimens were surface melted by the laser radiation focused to a 500-μm beam size and traversed at 0.5-40.0 cm/s to obtain melt layers with cooling rates of 10^2-10^5 °C/s.

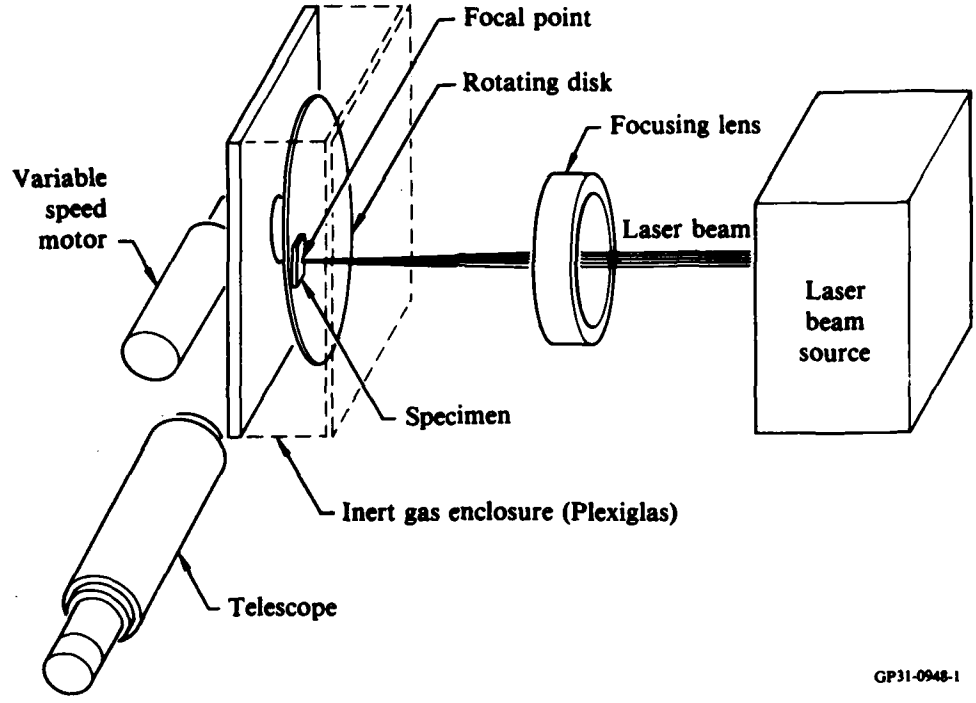

Figure 1. Experimental arrangement for laser-melting titanium alloys.

Selected titanium/rare-earth alloys were rapidly solidified by electron-beam melting and splat quenching. The apparatus shown in Figure 2, mounted in a vacuum chamber, was used to produce 50-500 g lots of rapidly solidified alloy flakes. The electron beam is focused onto a prealloyed Ti-alloy rod. The molten drops hit the rotating disk and are stretched into thin flakes under the combined actions of a high angular velocity and the centrifugal force of the rotating disk. The melt drop size and drip rate were controlled by varying the rotation speed of the alloy rod, vertical traverse rate of the rod, and power input to the alloy rod. The flake thickness was controlled by varying the speed of the rotating copper disk. The flakes produced by this method are particularly suited for transmission electron microscopic examination of as-solidified microstructures and microstructural modifications resulting from various annealing treatments.

2.2 Thermal Analysis of Laser Surface Melting of Ti-8Al

When the surface of a material is scanned by a high-power laser beam, the resulting temperature distribution, depth of melting, and cooling-rate distribution are related to the laser spot size, velocity, and power level.

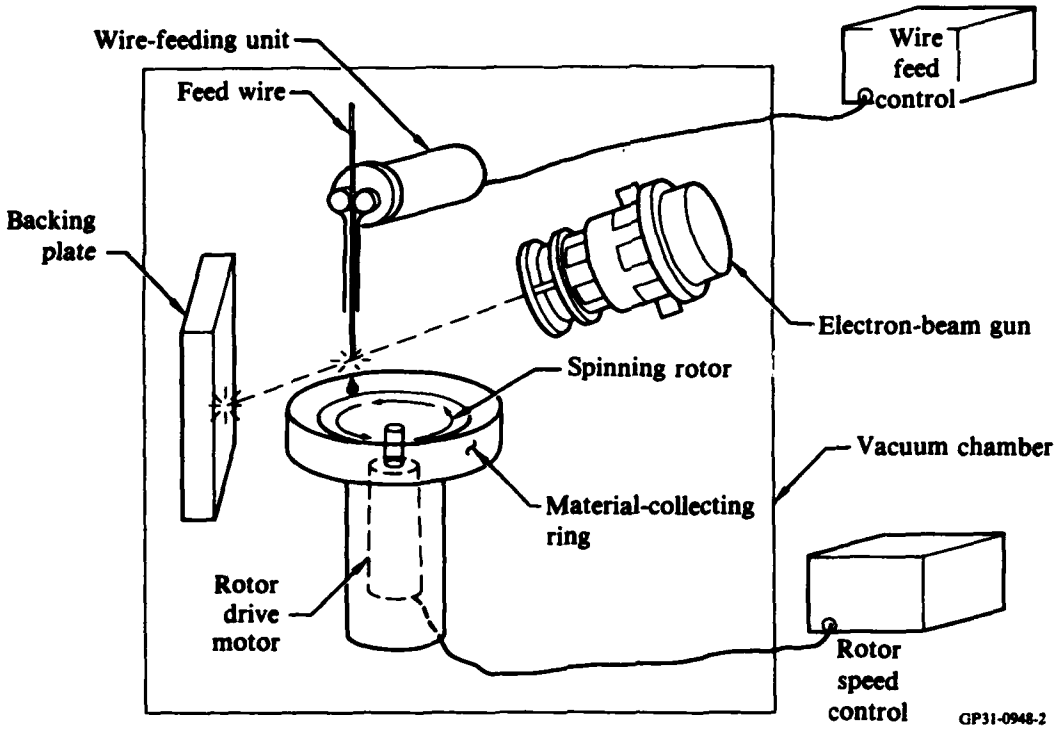

Figure 2. Experimental arrangement for producing rapidly solidified titanium alloy flakes.

If the laser beam power has a Gaussian distribution over the beam area, the temperature distribution in the material being irradiated is (References 6-8):

$$T(x,y,z) = \frac{P}{C_p DR} \cdot \frac{1}{\sqrt{2\pi^3}} \int_0^\infty \frac{e^{-H(u)}}{1+u^2}\, du, \qquad (1)$$

where

$$u^2 = 2Dt'/R^2 , \qquad (2)$$

$$H(u) = \frac{[(x/R + (\rho\tau/2)u^2]^2}{2\,(1+u^2)} + \frac{(z/R)^2}{2u^2} , \qquad (3)$$

$$\rho = RV/D, \qquad (4)$$

and C_p is the specific heat per unit volume, D is the thermal diffusivity, P is the total laser power absorbed, R is the laser beam spot radius, V is the speed of traversal of the laser beam, and t′ is a characteristic time. The liquidus isotherm is determined by setting Equation (1) equal to T_m, the melting temperature of the material, and the melt depth is given by

$$z_m = z_o \ln(P/P_m), \tag{5}$$

where P_m is the absorbed power just before melting occurs and z_o is a characteristic depth.

For Ti-8Al, $C_p = 2.19\ J \cdot K^{-1} \cdot cm^{-3}$ and $D = 0.048\ cm^2/s$. The calculated liquidus isotherms in the y-z plane of Ti-8Al when irradiated with a laser beam having P = 860 W are shown in Figure 3 for different laser-beam specimen-coupling efficiencies. The position of solid-liquid interfaces determined experimentally from the tranverse-section photomicrographs of laser-melted Ti-8Al are shown by dotted lines in Figures 3a and 3b. The positions of solid-liquid interfaces match the positions calculated for a specimen-beam coupling efficiency of 25%. The coupling efficiencies in other materials are typically 15-25% (References 6, 9, 10).

If the thermal gradient far from the center of the laser beam approaches that of a point source, the cooling rate can be calculated from the expression

$$\frac{\partial T}{\partial t} = - V \left(\frac{x}{r^2} + \frac{V}{2D} \left(1 + \frac{x}{r} \right) \right) T, \tag{6}$$

where

$$r^2 = x^2 + y^2 + z^2 \ . \tag{7}$$

Contours of constant cooling rates for different laser-beam traverse rates shown in Figure 4 indicate that cooling rates > 10^3 °C/s can be produced with a laser beam power > 860 W and a specimen traverse rate > 0.5 cm/s.

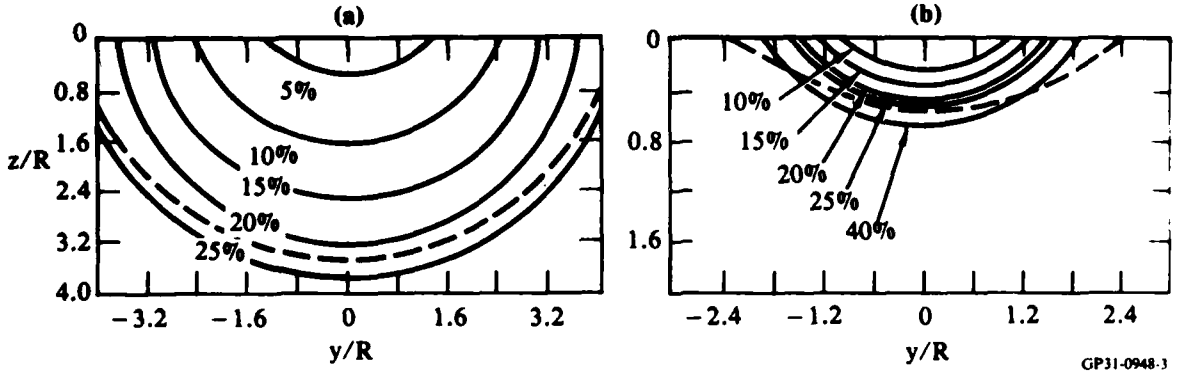

Figure 3. Laser-melting solid-liquid interfaces in Ti-8Al calculated for a laser-beam power of 860 W and different coupling efficiencies for laser-beam traverse rates of (a) 0.5 cm/s and (b) 5 cm/s. The experimentally determined interfaces are shown by dashed lines.

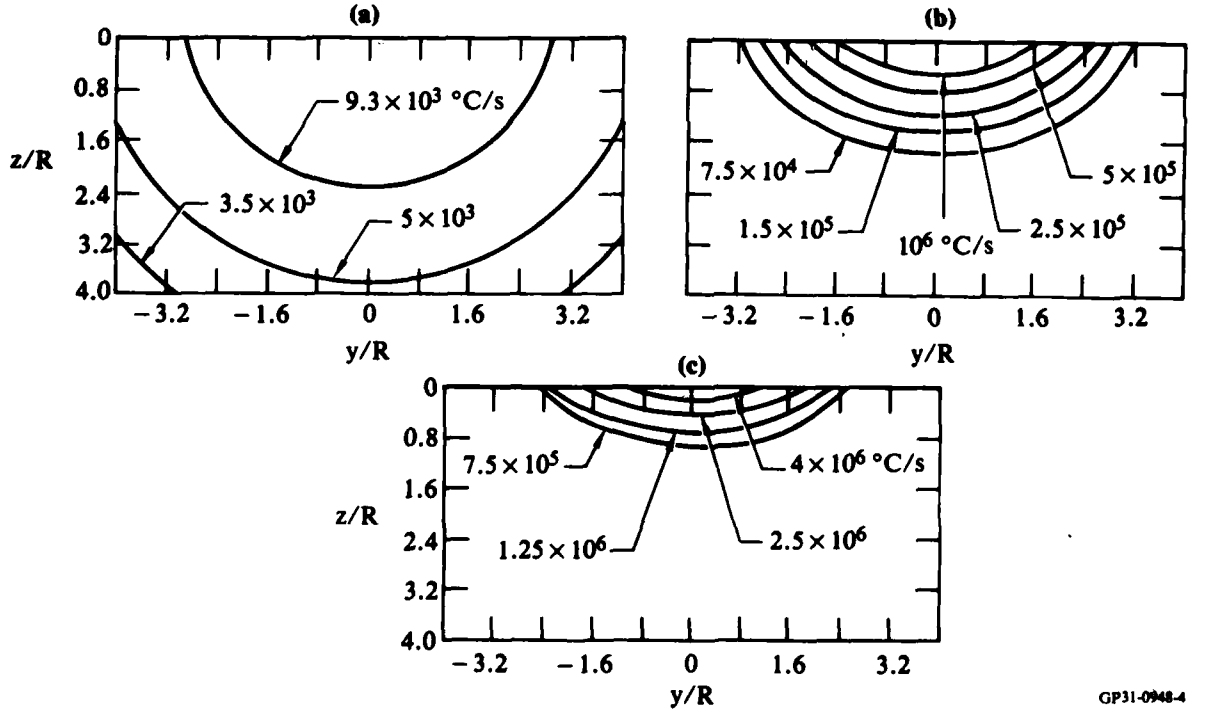

Figure 4. Equal cooling rate contours in laser-melted Ti-8Al calculated for a laser-beam power of 860 W, coupling efficiency of 25%, and traverse rates of (a) 0.5 cm/s, (b) 5.0 cm/s, and (c) 10 cm/s.

2.3 Topographical and Microstructural Characteristics of Laser-Melted Zones in Ti-8Al

The optical photomicrographs of laser-melted Ti-8Al and Ti-8Al-2.0Er alloys shown in Figure 5 reveal that the microstructures at low beam-scanning speeds consist of columnar grains, which change into equiaxed grains with increasing scanning speeds. At the center of the melt pool, the grains are elongated in the beam propagation direction. With increasing distance from the center of the melt pool, the angle between the long direction of the grains and the beam propagation direction increases, in agreement with the predicted rotation of the growth vector from the beam-scan direction at the center of the pool to a direction nearly perpendicular to the side of the pool at the perimeter.

The microstructures also reveal that the alloys undergo $\beta \rightarrow \alpha'$ martensitic transformation during rapid solidification, with individual grains containing more than one crystallographic orientation of martensite. Both the martensite packet size and plate length decrease with increasing laser-beam traverse speed.

Figures 6a, 6b and 6c are the scanning and transmission electron micrographs of a Ti-8Al-0.5Y alloy surface melted by an incident heat flux of 4.2 MW/cm^2 from a continuous CO_2 laser source. Whereas the microstructure of conventionally cast alloy (Region A in Figure 6a) consists of coarse, equilibrium, Y-rich particles, laser melting at fast sweep rates results in a redissolution of coarse particles and homogeneous precipitation of fine, 100-200 nm diameter dispersoids (Figures 6b and 6c). The microstructural homogeneity increases and the second-phase dispersoid size decreases with increasing specimen sweep rate, and hence with increasing solidification rate.

Figures 7a-7f are scanning electron micrographs of conventionally cast and laser-melted Ti-8Al-Y and Ti-8Al-Er alloys. The scanning electron micrographs of conventionally cast Ti-8Al-RE alloys in Figures 7a-7c show bimodal distributions of coarse 1-5 μm diameter particles, which precipitated from the liquid, and fine 10-20 nm diameter dispersoids, which probably formed by solid-state precipitation. In the laser-melted regions, the coarse particles are absent, and the microstructures contain large amounts of homogeneously dispersed, spherical, 10-20 nm diameter, second-phase dispersoids as shown in Figures 7d-7f. Annealing for 1 h at 800°C or 900°C does not significantly

alter the dispersoid size and distribution. The dispersed-phase parameters in the laser-melted layers and the corresponding theoretical Orowan strengthening contributions are listed in Table 1. The closely spaced, fine dispersoids resulting from laser melting are calculated to produce 227-355 MPa strength increments in Ti-8Al.

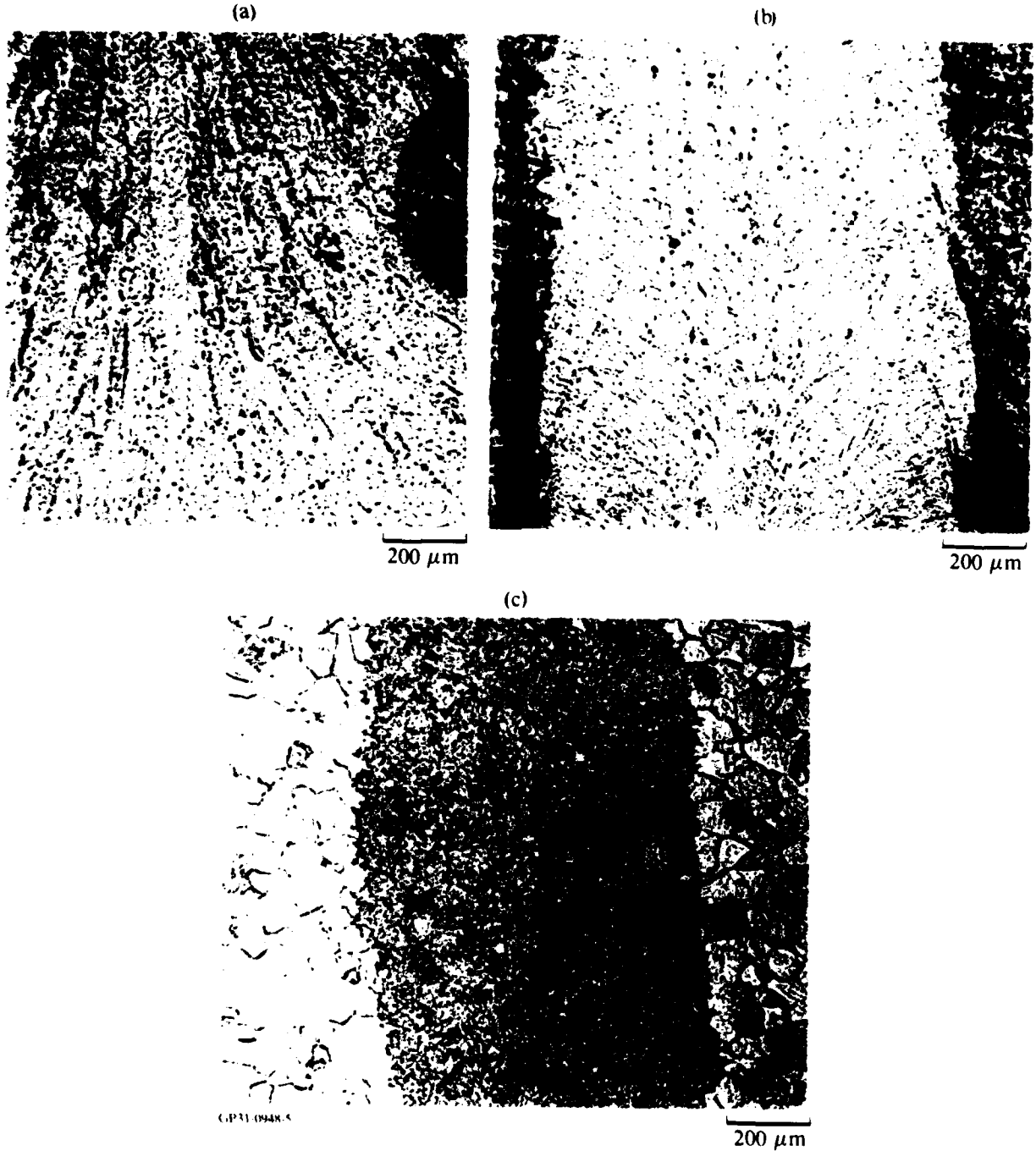

Figure 5. Microstructures of Ti-8Al-2.0Er laser-melted at a traverse rate of (a) 0.5 cm/s and (b) 10 cm/s, and (c) Ti-8Al at 30 cm/s with a 250-μm radius, 860-W laser beam.

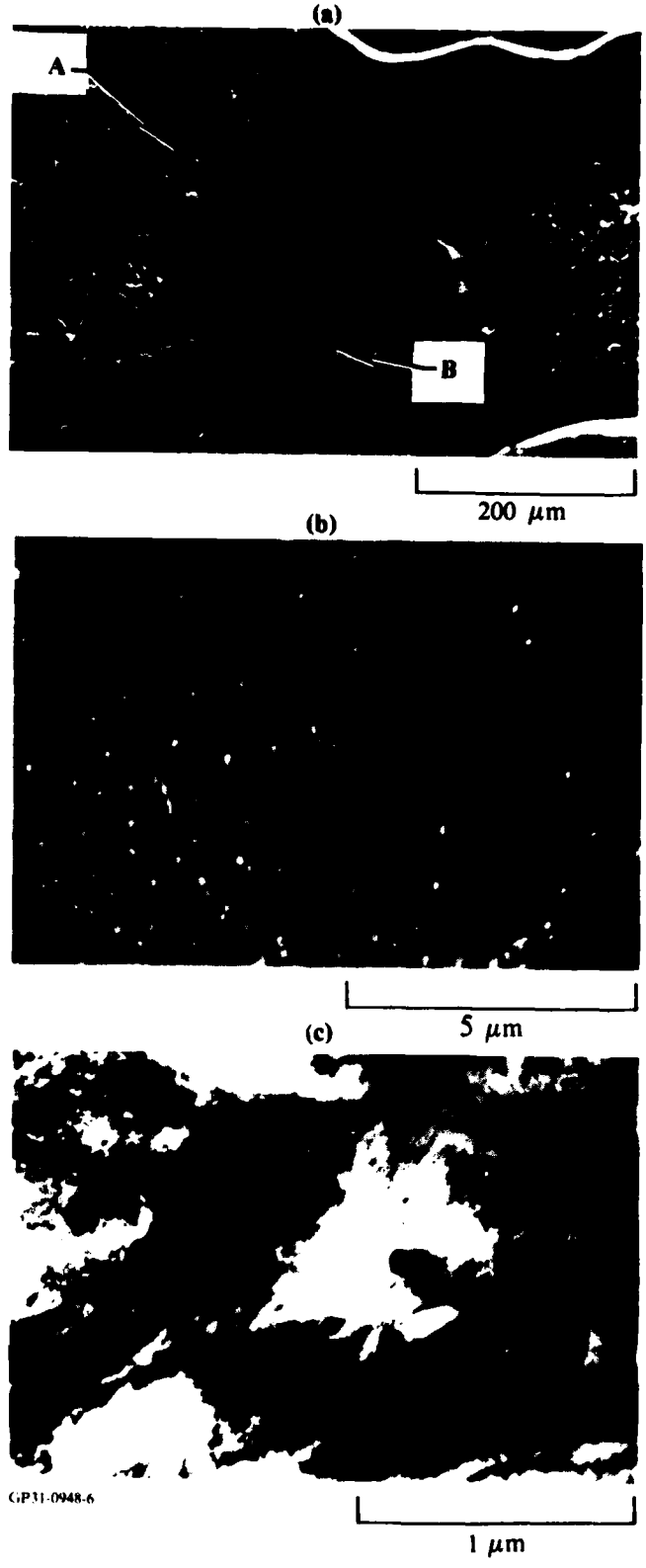

Figure 6. Microstructures of laser-melted Ti-8Al-0.5Y; (a) low-magnification photomicrograph showing coarse particles in the as-cast alloy (Region A) and dissolution of the particles in the laser-melted area (Region B), (b) scanning electron micrograph showing fine dispersoids in the laser-melted region, and (c) transmission electron micrograph of martensitic phase and fine dispersoids in the laser-melted region.

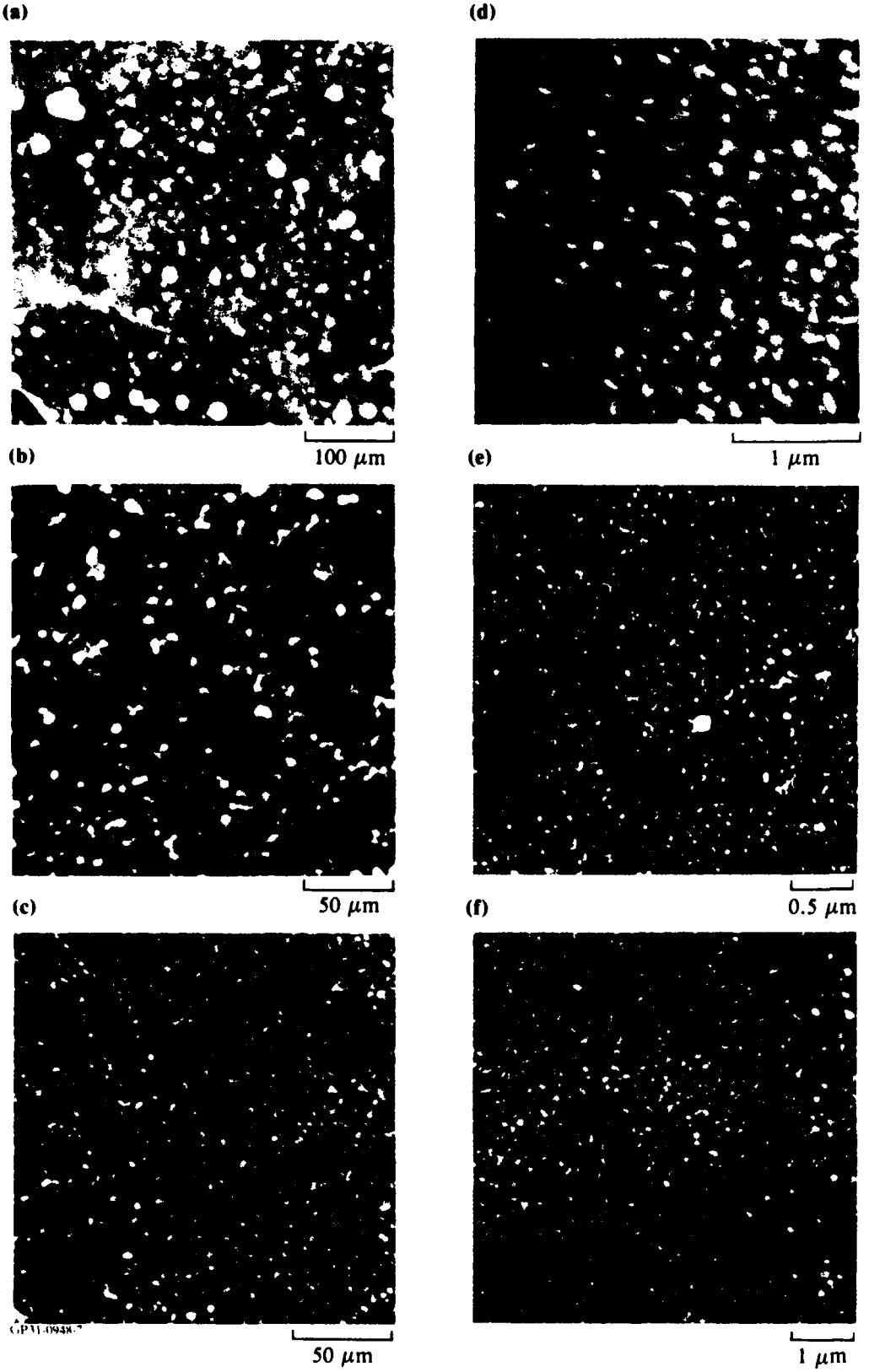

Figure 7. Scanning electron micrographs of conventionally melted ingots of (a) Ti-8Al-0.5Y, (b) Ti-8Al-1.0Y, and (c) Ti-8Al-2.0Er and laser-melted surfaces of (d) Ti-8Al-0.5Y, 40 cm/s, (e) Ti-8Al-1.0Y, 30 cm/s, and (f) Ti-8Al-2.0Er, 40 cm/s with a 250-μm radius, 860-W laser beam.

TABLE 1. DISPERSOID PARAMETERS AND CALCULATED STRENGTH INCREMENTS IN Ti-8Al-1.0Y, Ti-8Al-2.0Y, AND Ti-8Al-1.5Er ALLOYS RAPIDLY SOLIDIFIED AND ANNEALED AT 700°C FOR 2 h.

Alloy	Dispersoid diameter (nm)	Interparticle spacing, L (μm)	Strength increment, σ (MPa)
Ti-8Al-1.0Y	59	0.98	300
Ti-8Al-2.0Y	75	0.88	355
Ti-8Al-1.5Er	52	1.25	227

GP31-0948-29

The refinement of dispersoids in a laser-melted alloy results from a reduced time for coarsening during solidification and from the higher-than-equilibrium solid solubility of Er and Y in Ti-8Al with subsequent solid-state precipitation of the dispersoids. The high volume fractions of the dispersoids indicate that the dispersoids are titanium-rich Ti-Y and Ti-Er intermetallic compounds rather than pure Y, Er, or oxide dispersions. These compounds are probably metastable phases because the equilibrium phase diagrams for Ti-Y and Ti-Er do not show the existence of any intermetallic compound phases (Reference 11). The precise compositions of the dispersoids is relatively unimportant in their influence on alloy mechanical behavior. The important factors are the small size of the dispersed particles and their stability at high temperatures, where they can influence and modify alloy behavior. The results of this study demonstrate the feasiblity of producing dispersion-strengthened Ti alloys by rapid solidification.

2.4 Laser Surface Alloying of Titianium with Yttrium and Erbium

Titanium specimens, coated with 0.02 to 2-μm thick electron-beam-evaporated yttrium and erbium metal-films were surface melted using a 1.5 kW, continuous-wave, CO_2 laser beam at traversing speeds of 0.5 to 40 cm/s. The microstructures of the laser-melted regions, determined by scanning and transmission electron microscopy, were correlated with the laser-processing parameters.

Figures 8a-8c are scanning electron micrographs of transverse sections of the laser-melted Ti-Y alloy at laser-beam traversing speeds of 0.5, 5, and 30 cm/s respectively. The positions of the solid-liquid interfaces match the

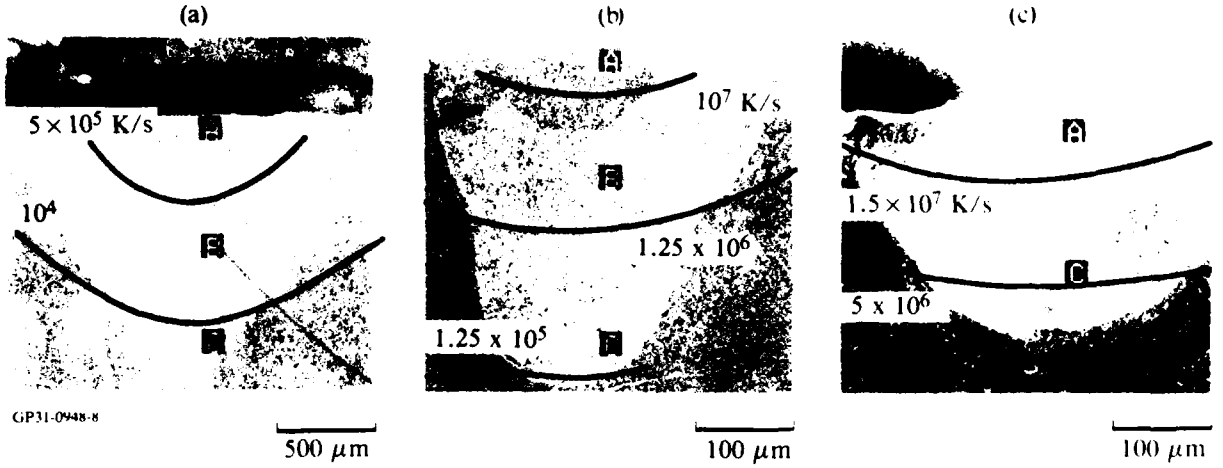

Figure 8. Cross-sectional views of laser-melted Ti-Y at specimen traverse speeds of (a) 0.5, (b) 5, and (c) 10 cm/s. Calculated cooling rates are indicated on the photographs.

theoretically predicted melting isotherms for a specimen-beam coupling efficiency of 25%. Constant cooling-rate curves, calculated from the heat transfer model for a rapidly moving, high-power, Gaussian source, are included in Figures 8a-8c. In the laser-melted Ti-RE alloys with the 0.2-μm thick rare-earth films, the microstructure consists of fine 10-20 nm dispersoids. The dispersoid size decreases with increasing laser-beam traversing speed as well as with increasing distance from the specimen surface. The volume fraction of the dispersoids increases with increasing film thickness and melt depth. The equilibrium, coarse, constituent particles, which are generally observed in conventionally cast Ti alloys containing corresponding amounts of rare-earth elements, were absent in the laser-melted alloy. Figures 9a-9c are transmission electron micrographs of dispersoids in the laser-melted Ti-Y alloys. The second-phase dispersoids were not observed in Ti-RE samples with 0.02-μm thick films.

2.5 Thermal Stability of Dispersoids in Ti-Al-Y and Ti-Al-Er Alloys

Figures 10 and 11 show the microstructures of rapidly solidified and differently annealed Ti-8.0Al-Y and Ti-8.0Al-Er alloys. The rapidly solidified Ti-8.0Al-1.0Y alloy has a martensite structure with fine, incoherent dispersoids. However, the Ti-8Al alloy containing 2.0 wt% Y has a fine, equiaxed grain structure with ~ 100-nm diameter dispersoids. Annealing at 600°C results in the formation of fine, coherent, ordered Ti_3Al precipitates with no

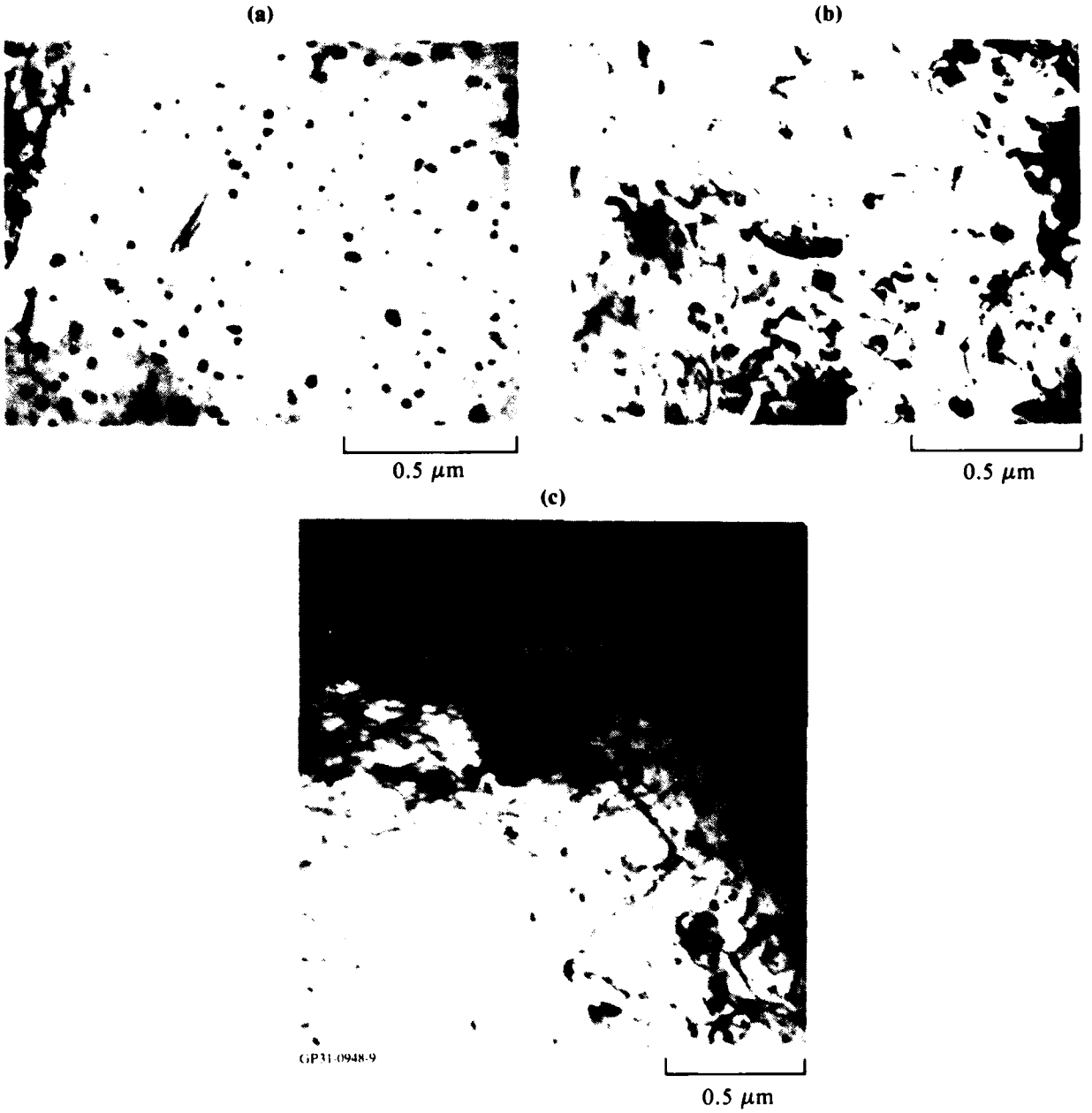

Figure 9. Transmission electron photomicrographs of dispersoids in Ti-Y alloy laser-melted at an incident power of 860 W and specimen traverse rate of 10 cm/s; (a) bright-field micrograph of dispersoids, (b) and (c) bright-field micrographs of dislocation-dispersoid interactions.

appreciable coarsening of Y-containing dispersoids. The rapidly solidified Ti-8.0Al-Er alloys have equiaxed 1-2 μm grains and ~ 50-100 nm incoherent dispersoids. The grains and dispersoids do not coarsen appreciably upon annealing at 600-930°C.

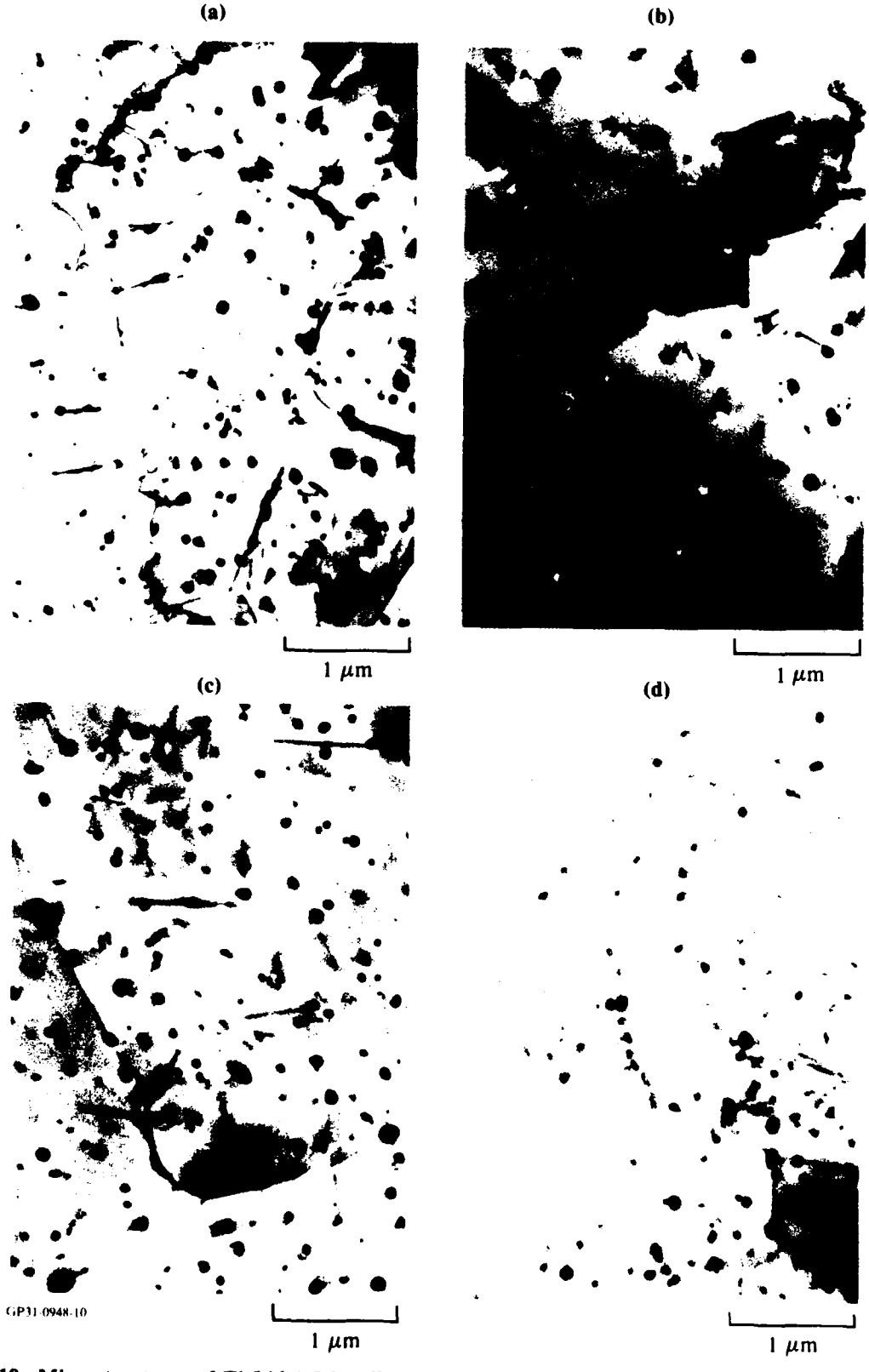

Figure 10. Microstructures of Ti-8Al-1.5 Er alloy (a) rapidly solidified, (b) annealed at 600°C for 24 h, (c) annealed at 825°C for 16 h, and (d) annealed at 930°C for 3 h.

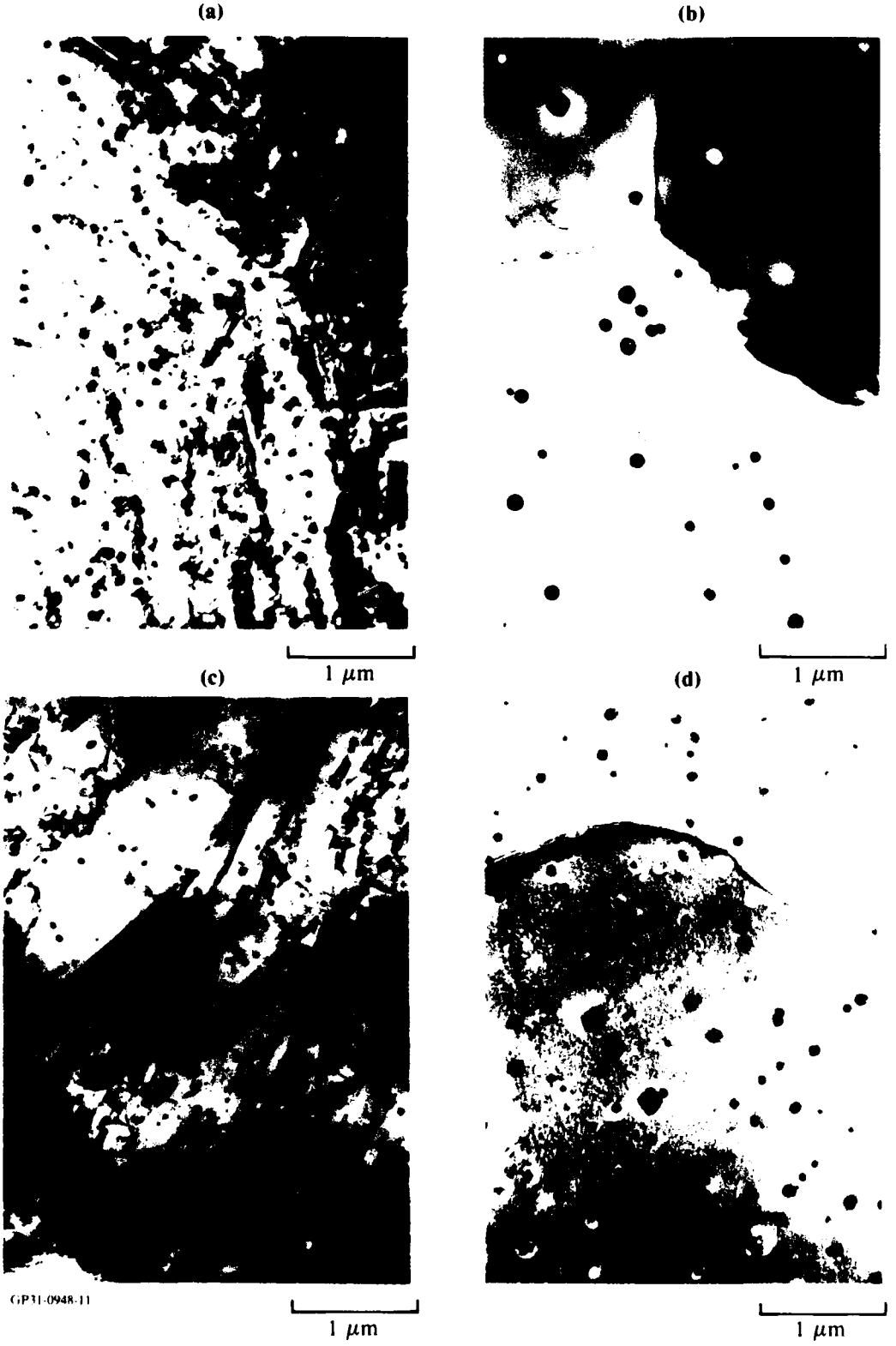

Figure 11. Microstructures of (a) rapidly solidified Ti-8Al-1.0Y alloy, (b) rapidly solidified Ti-8Al-2.0Y alloy, (c) Ti-8Al-1.0Y alloy annealed at 600°C for 4 h, and (d) Ti-8Al-2.0Y alloy annealed at 600°C for 24 h.

2.6 Strength and Ductility Improvements in Ti-8Al-Y and Ti-8Al-Er Alloys

Plastic deformation in Ti-Al alloys containing Ti_3Al (α_2) precipitates occurs by the shearing of α_2 precipitates by glide dislocations, resulting in the formation of antiphase boundaries (APB) on the slip planes within the particles. The movement of a second dislocation removes the disorder created by the first, and the slip thus becomes confined to narrow, widely spaced, planar bands. The planar slip bands cause stress concentrations at grain boundaries and slip-band intersections, which become potential crack nucleation sites in the early stages of deformation. Flow stress in the alloys is dependent on the coherency strains, the APB energy of α_2, and the volume fraction of α_2 precipitates.

Incoherent dispersoids introduced into a Ti-Al alloy containing α_2 precipitates can modify the slip behavior by their influence on dislocation sources as well as by acting as barriers to dislocation motion. Dislocations overcome the dispersed-phase particles by the Orowan bypass (Reference 12) and Hirsch cross-slip (Reference 13) mechanisms, which result in greater densities of localized dislocation channels during the initial stages of deformation. With increasing deformation, dislocations are swept into the channels, resulting in well-defined cells whose spacing is determined by the spacing of the initial localized channels. Thus, the dispersoids homogenize the slip and refine the substructure formed during deformation, and these effects of dispersoids can improve ductility.

In the presence of a bimodal distribution of particles, the overall flow stress is governed by a superposition of the flow stresses attributable to the two kinds of obstacles. Thus, by incorporation of incoherent rare-earth dispersoids, improvements in ductility as well as strength can be obtained. The strength increment from a distribution of dispersoids with particle diameter x and interparticle spacing L is given by the relation

$$\tau = \frac{1.06\ Gb}{2\ \Pi\ L} \ln \frac{x}{4b}\ , \tag{8}$$

where G is the shear modulus of the matrix and b is the Burgers vector of the dislocations. The experimentally determined values of x and L and the calculated Orowan stresses for Ti-8.0Al-Y and Ti-8Al-Er alloys are summarized in Table 1.

The possibility of improving the room-temperature ductility by grain refinement has been demonstrated for a precipitation-strengthened Ti-Al alloy (Reference 14). A significant improvement in the strength and ductility of a Ti-Al alloy was observed when the grain size was decreased from 90 μm to 9 μm. With decreasing grain size, the dislocation pile-up length is reduced and the grain boundary sources are increased. Consequently, the stresses caused by dislocation pile-ups are not high, and the specimens can accommodate higher strain. Because the dispersoids inhibit grain-growth, the fine-grain microstructure of rapidly solidified Ti-8Al-Y and Ti-8Al-Er alloys should have higher ductility than Ti-8Al alloys.

The dispersoids inhibit recrystallization and retard grain growth at elevated temperatures, thus enabling potential improvements in high-temperature properties.

An additional beneficial effect of the incoherent dispersoids is the improvement in creep resistance. Creep strengthening by the precipitation of stable intermetallic precipitates has been demonstrated in γ'-strengthened nickel-base superalloys (Reference 15). Creep characteristics of α_2-precipitation-strengthened Ti-8Al and Ti-10Al alloys indicate that the presence of α_2 precipitates reduces the creep rates considerably (Reference 4). Improved creep resistance of the alloys containing coherent, ordered precipitates arises from the high elastic modulus of the ordered phase, large coherency strains between the matrix and precipitates, and low diffusion rates in the ordered phase. The presence of incoherent dispersoids further increases the creep strength and reduces the creep rate by stabilizing dislocation substructures and creating internal stresses that must be overcome in the dislocation multiplication process.

2.7 Summary of Rapid Solidification Processing of Ti-Al-Y and Ti-Al-Er Alloys

Rapid solidification at cooling rates > 10^4 K/s results in homogeneously distributed, closely spaced, 10-100 nm diameter, incoherent dispersoids in Ti-8Al-1.0Y, Ti-8Al-2.0Y, and Ti-8Al-1.5Er. The dispersoids do not undergo appreciable coarsening at 600-900°C. The dispersoids produce a 30-60% strength increase in Ti-8Al alloys. The 10-100 nm dispersoids produced by rapid solidification disperse planar slip and increase the ductility of precipitation-strengthened Ti-8Al alloy.

3. EFFECTS OF YTTRIUM AND YTTRIA ADDITIONS ON SUPERPLASTIC DEFORMATION OF Ti-6Al-4V AND Ti-6Al-2Nb-1Mo-0.8Ta

3.1 Beneficial Effects of Yttrium and Yttria Additions on Superplasticity of Ti Alloys

The main requirements for superplastic deformation of alpha+beta titanium alloys are $T/T_\beta > 0.85$, where T is the deformation temperature and T_β is the beta transus temperature, 5-10 μm size equiaxed grains, and slow grain growth at the superplastic forming temperatures (Reference 16). The superplastic strain rate at a constant applied stress and the strain-rate sensitivity of flow stress increase with increasing T/T_β and decreasing grain size (Reference 16). The grain growth occurring at superplastic forming temperatures results in an increase in flow stress and a decrease in strain-rate sensitivity of flow stress with time. Because of the grain refinement and grain-growth retardation effects of Y and Y_2O_3 in Ti alloys, the additives are expected to improve the superplastic formability of Ti-6Al-4V.

In this part of the investigation, the improvements in superplastic formability effected by the additions of Y and Y_2O_3 to Ti-6Al-4V and Ti-6Al-2Nb-1Mo-0.8Ta were determined.

3.2 Superplastic Forming Evaluation of Ti-6Al-2Nb-1Mo-0.8Ta-Y Alloys

The superplastic formability of Ti-6Al-2Nb-1Mo-0.8Ta, Ti-6Al-2Nb-1Mo-0.8Ta-0.01Y, Ti-6Al-2Nb-1Mo-0.8Ta-0.025Y, and Ti-6Al-2Nb-1Mo-0.8Ta-0.01Y_2O_3 was evaluated using the cone-forming tester shown in Figure 12 and conical die shown in Figure 13. This test enables the cone depth and strain to be measured as the specimen is being superplastically formed under the action of biaxial stress (Reference 17). The biaxial stress (σ) for an applied gas pressure (p) is given by

$$\sigma = \frac{\gamma p}{2t} \tag{9}$$

where t is the membrane thickness and γ is the radius of curvature of the membrane. For a cone angle of 58°, the ratio of thickness to radius of curvature, t/γ, is approximately constant as the cone forms, and hence forming

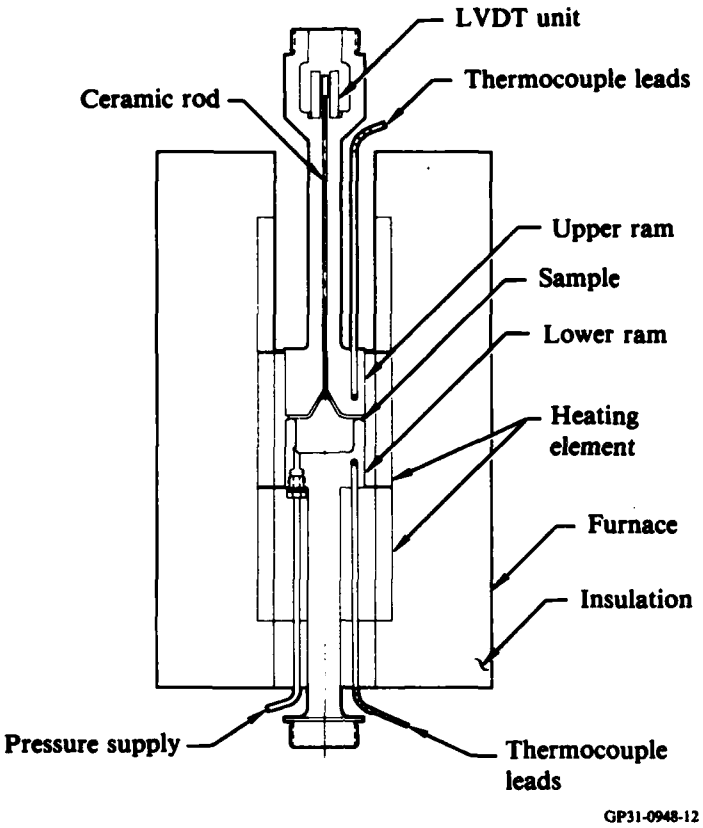

Figure 12. Experimental arrangement for laboratory cone-forming tests.

occurs under a constant stress mode, provided that the pressure is maintained constant. The strain at any instant is given by

$$\varepsilon = \ln(t/t_o) \ . \tag{10}$$

The strain is related to the cone depth by the relation

$$\varepsilon = 0.30 - \ln \frac{1 - q_2}{1 - q_1} \tag{11}$$

where q_1 is the cone depth when contact is first made with the die, q_2 is the instantaneous cone depth, and 1 is the total depth of the conical die.

A cross-section of the test set up is shown in Figure 12. The test procedure consists of clamping a sample disk between the two rams, applying a nominal pressure on both surfaces of the sample, and heating the sample and rams to the forming temperature. Once thermal equilibrium is reached, the pressure is released on the cone side and increased to the testing value on

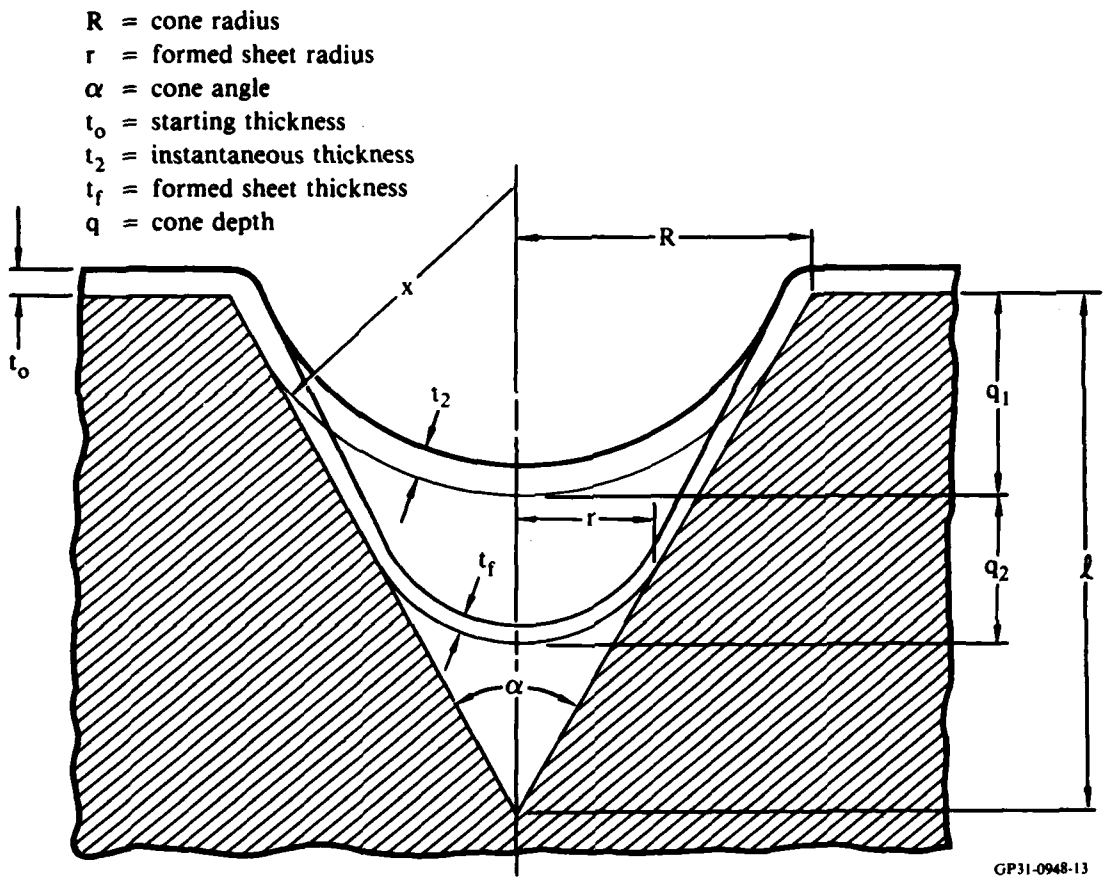

Figure 13. Cross section of conical die for superplastic-forming evaluation.

the other side. The movement of the tip of the cone as a function of time is monitored by the linear variable differential transformer (LVDT) unit. Stress and strain are calculated using Equations 9 and 11. The time dependences of cone height and strain rate are measures of the superplastic formability of the material.

Photographs of the cones and cross sections of the cones superplastically formed at 850 and 900°C are shown in Figures 14-17. The cone heights are larger and the cone cross-sections are more uniform for Ti-6Al-2Nb-1Mo-0.8Ta-Y alloys than for Ti-6Al-2Nb-1Mo-0.8Ta and Ti-6Al-2Nb-1Mo-0.8Ta-Y_2O_3 alloys. The superplastic strain rates shown in Figures 18 and 19 indicate that the superplastic formability of Ti-6Al-2Nb-1Mo-0.8Ta is improved by yttrium additions. The improved superplasticity results from smaller initial grain size and grain-growth retardation by Y dispersoids (Figures 20 and 21).

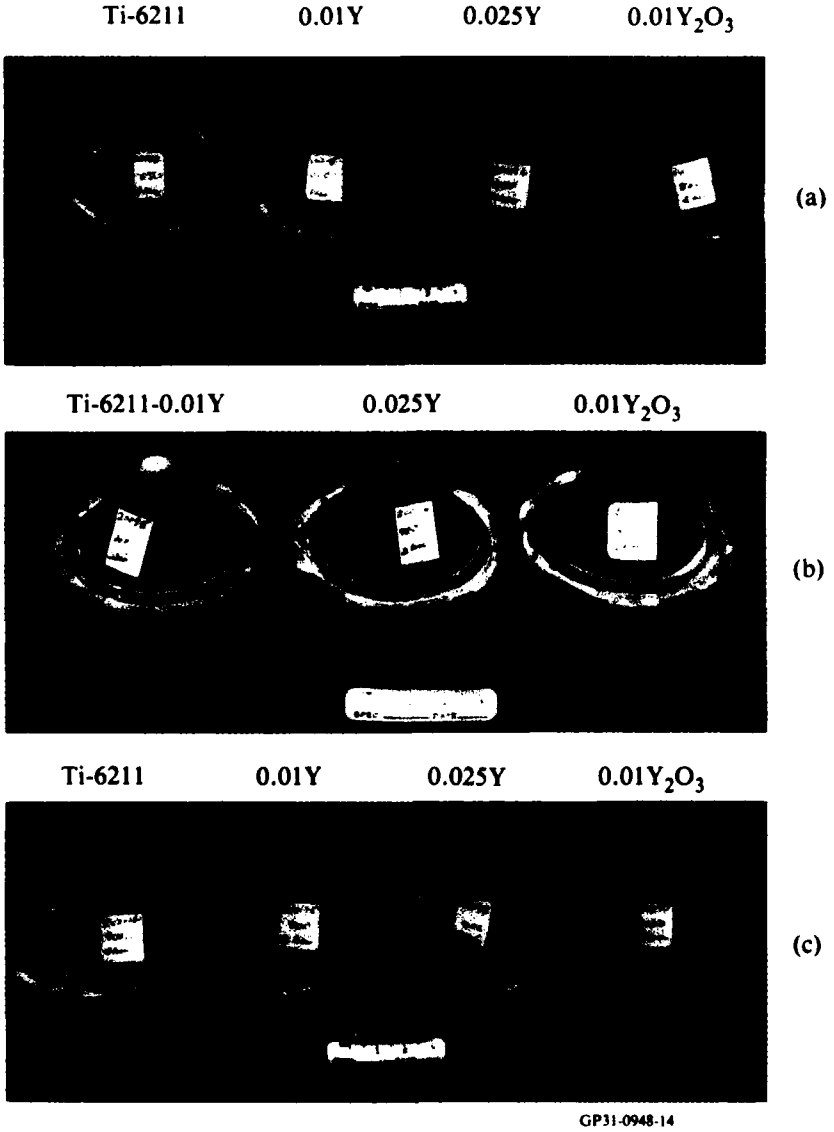

Figure 14. Superplastically formed Ti-6Al-2Nb-1Mo-0.8Ta-Y cones formed at (a) 850°C, 28 MPa, (b) 900°C, 16 MPa, and (c) 900°C, 28 MPa.

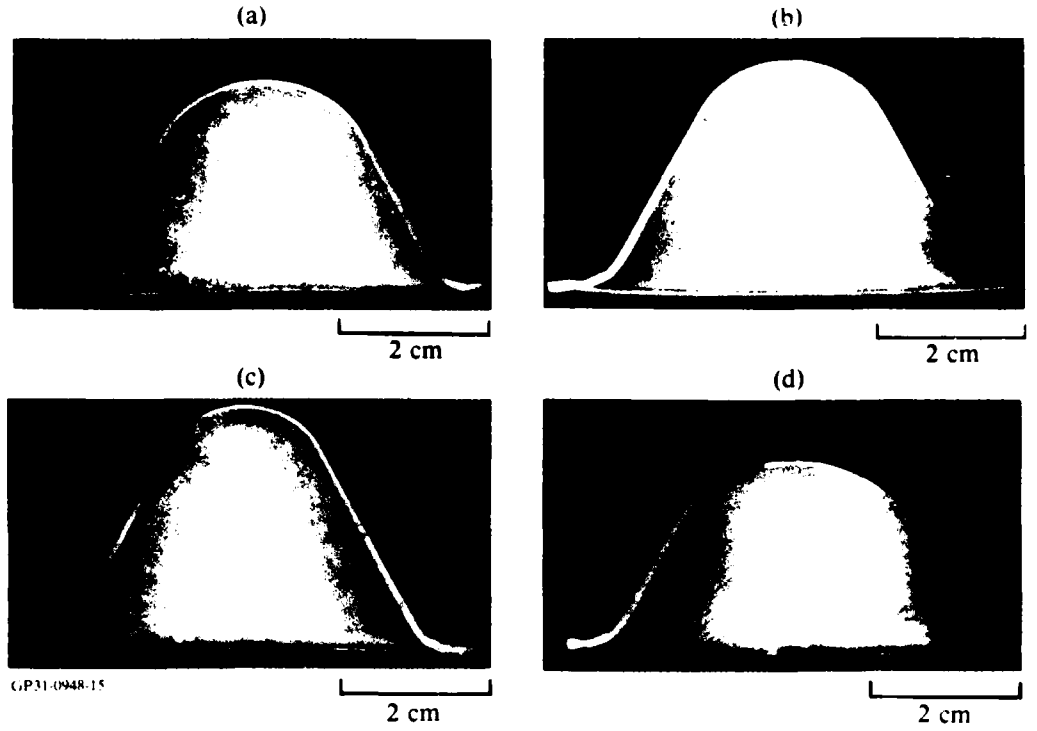

Figure 15. Cross sections of Ti-6Al-2Nb-1Mo-0.8Ta-Y cones superplastically formed at 850°C, 28 MPa; (a) Ti-6Al-2Nb-1Mo-0.8Ta, (b) Ti-6Al-2Nb-1Mo-0.8Ta-0.01Y, (c) Ti-6Al-2Nb-1Mo-0.8Ta-0.025Y, and (d) Ti-6Al-2Nb-1Mo-0.8Ta-0.01Y_2O_3.

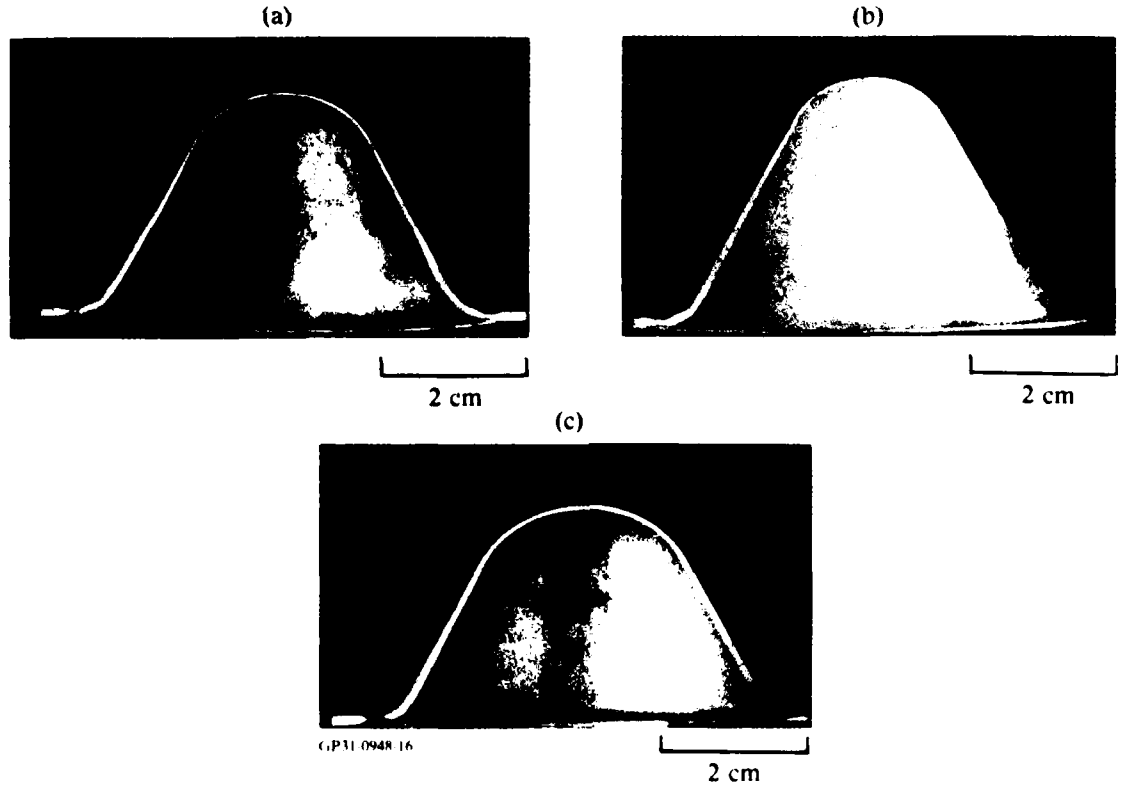

Figure 16. Cross sections of Ti-6Al-2Nb-1Mo-0.8Ta-Y cones superplastically formed at 900°C and 14 MPa; (a) Ti-6Al-2Nb-1Mo-0.8Ta-0.01Y, (b) Ti-6Al-2Nb-1Mo-0.8Ta-0.025Y, and (c) Ti-6Al-2Nb-1Mo-0.8Ta-0.01Y_2O_3.

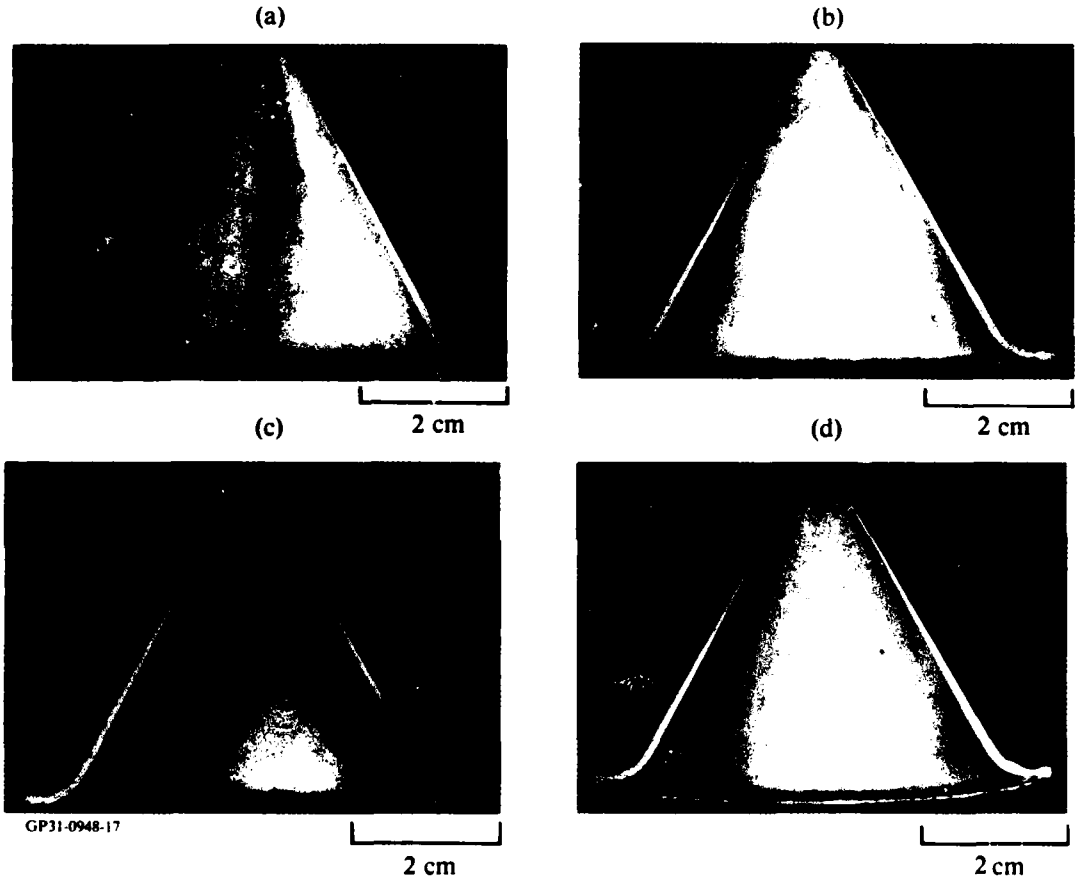

Figure 17. Cross sections of Ti-6Al-2Nb-1Mo-0.8Ta-Y cones superplastically formed at 900°C and 28 MPa; (a) Ti-6Al-2Nb-1Mo-0.8Ta, (b) ti-6Al-2Nb-1Mo-0.8Ta-0.01Y, (c) Ti-6Al-2Nb-1Mo-0.8Ta-0.02Y, and (d) Ti-6Al-2Nb-1Mo-0.8Ta-0.01Y_2O_3.

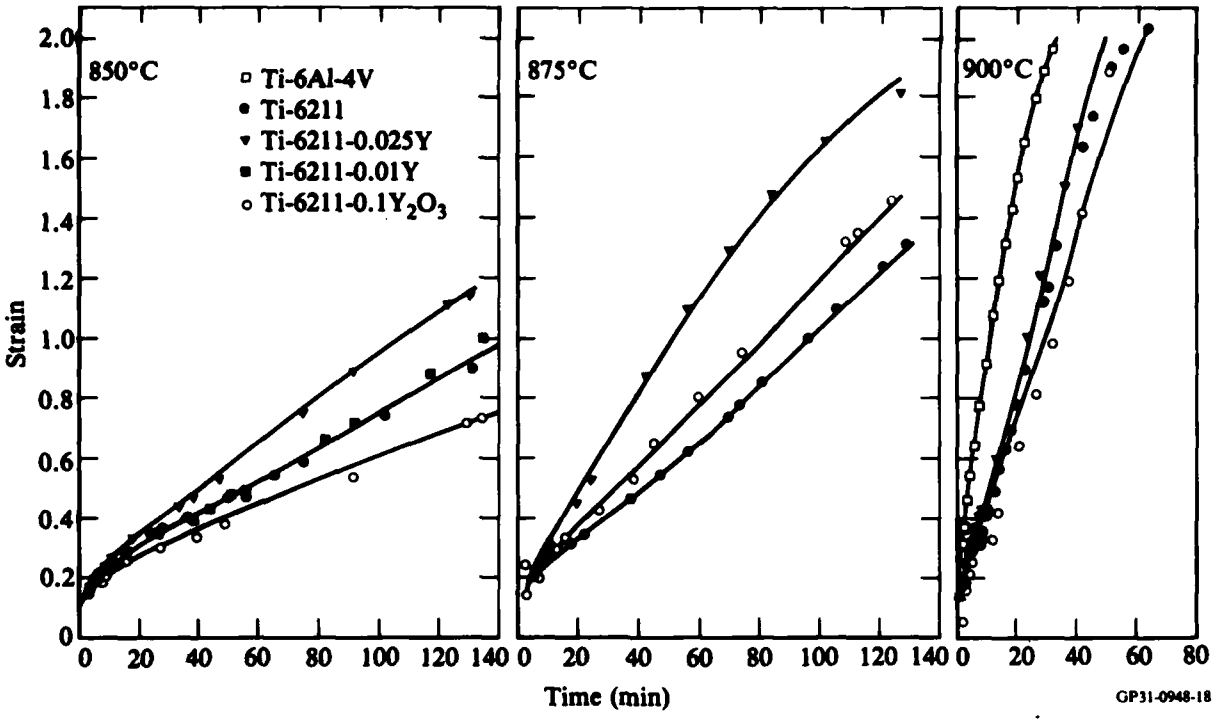

Figure 18. Superplastic strain-rates of Ti-6Al-2Nb-1Mo-0.8Ta-Y alloys at 28 MPa.

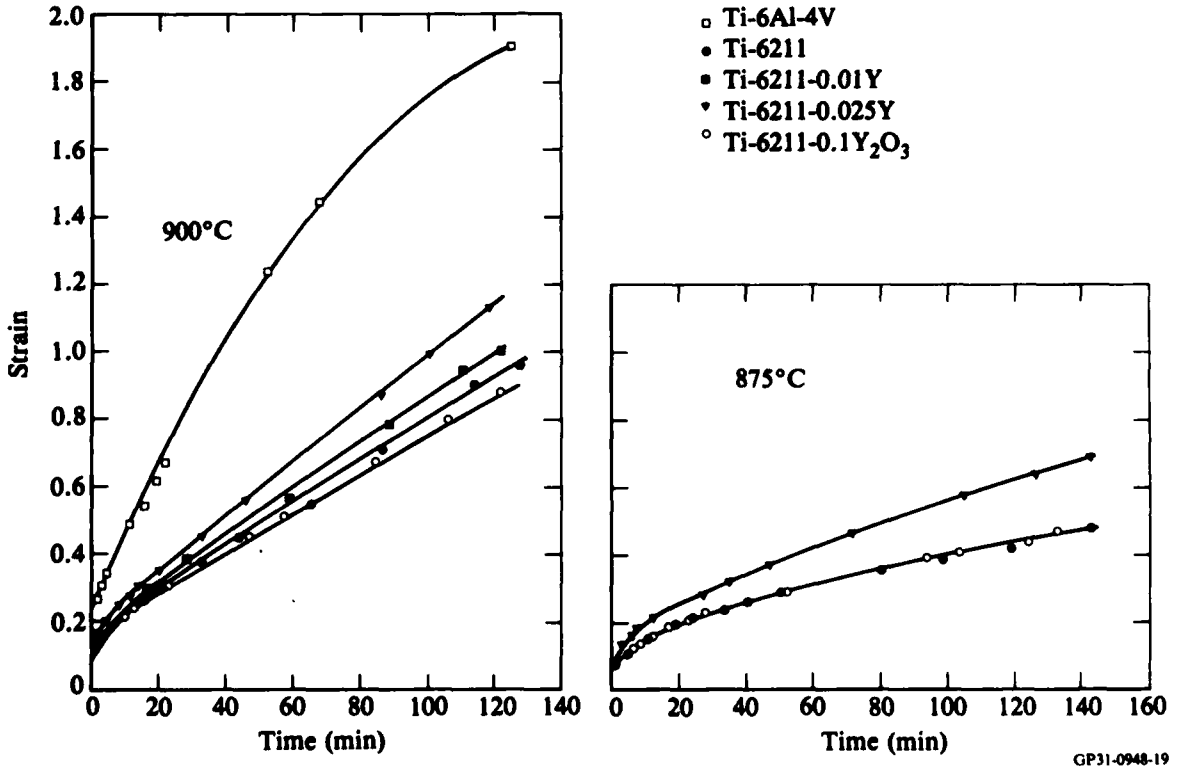

Figure 19. Superplastic strain-rates of Ti-6211-Y alloys at 14 MPa.

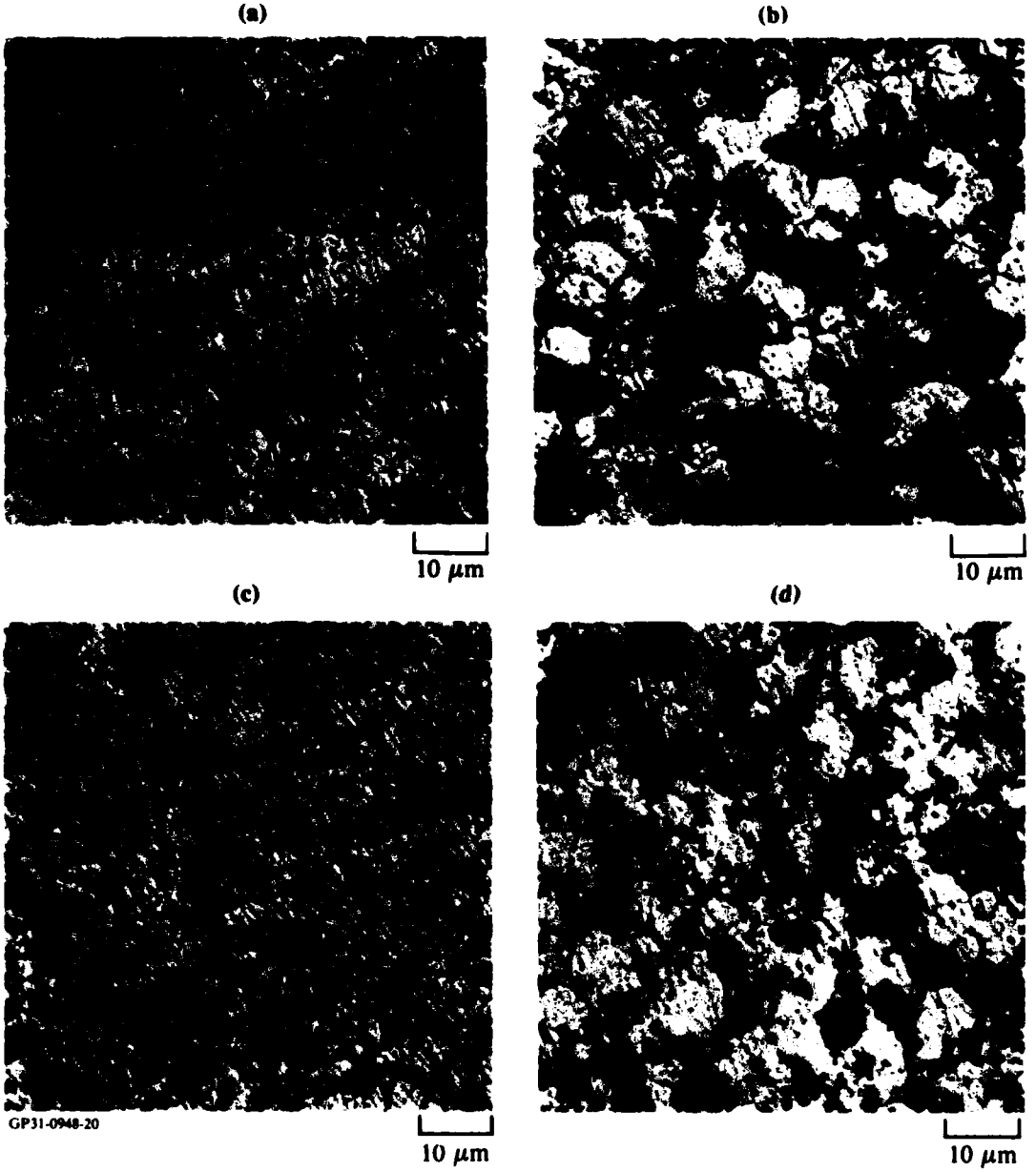

Figure 20. Microstructures of hot-rolled Ti-6Al-2Nb-1Mo-0.8Ta-Y alloys (a) Ti-6211, (b) Ti-6211-0.01Y, (c) Ti-6211-0.025Y, and (d) Ti-6211-0.01Y_2O_3.

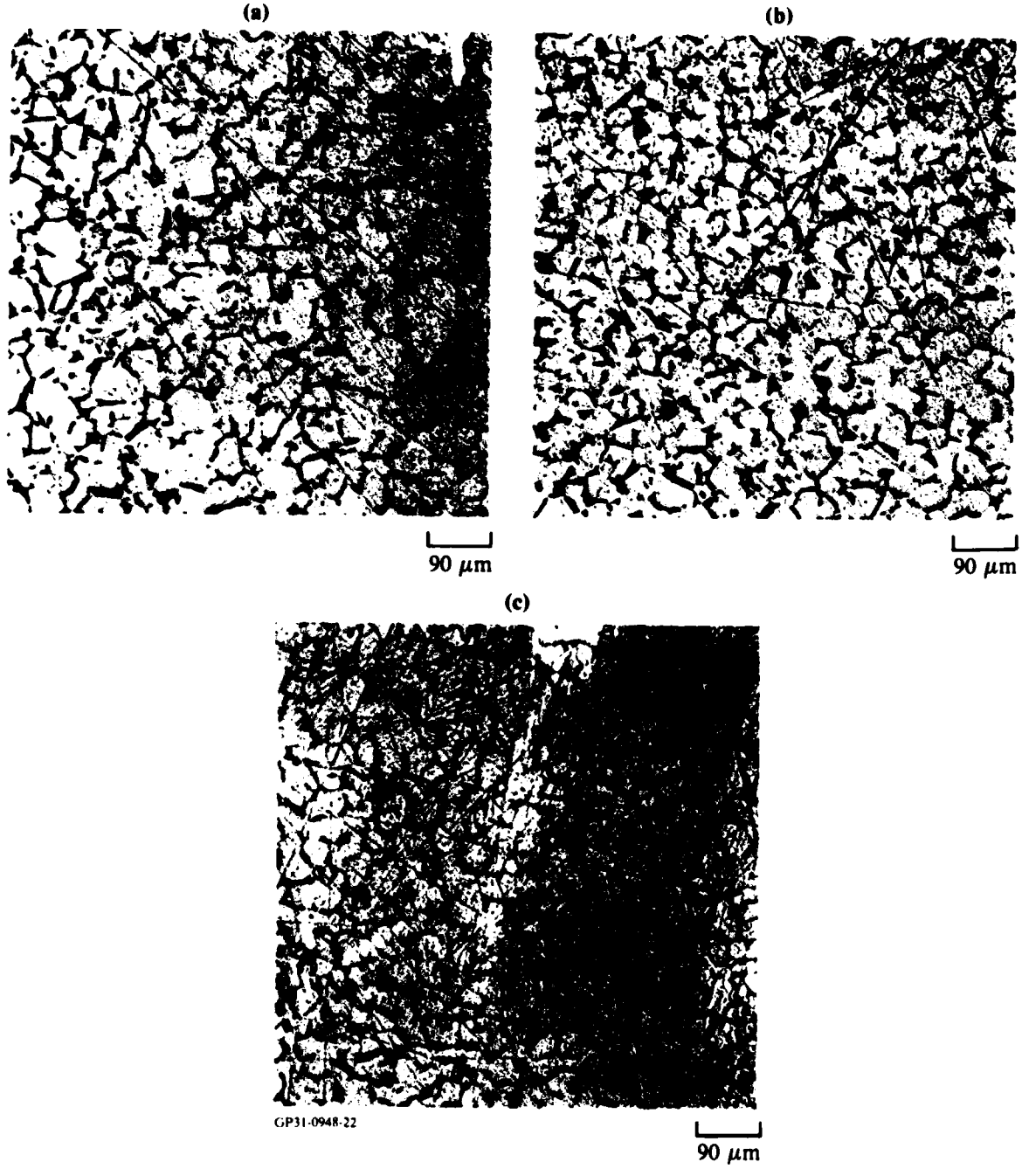

Figure 21. Microstructures of Ti-6Al-2Nb-1Mo-0.8Ta-Y alloys superplastically formed for 2 h at 900°C and 14 MPa, (a) Ti-6211, (b) Ti-6211-0.025Y, and (c) Ti-6211-0.01Y_2O_3.

3.3 Superplastic Forming Evaluation of Ti-6Al-4V-Y Alloys

The effects of Y additions on flow stress and strain rate sensitivity of Ti-6Al-4V at 906°C are shown in Figures 22a and 22b. The Y-containing Ti-6Al-4V has a lower flow stress and higher strain-rate sensitivity than standard Ti-6Al-4V at 906°C. The beneficial effects of Y additions arise from reduction in interstitial oxygen as a result of scavenging of oxygen by yttrium and grain-growth retardation by Y dispersoids. The lower concentration of interstitial oxygen produces lower flow stresses and higher strain-rate sensitivity and forming rates (Reference 16). The fine-grains, produced by pinning of grain boundaries by Y dispersoids, significantly decrease the flow stress and increase superplastic strains.

3.4 Summary of Superplastic Formability of Ti-6Al-2Nb-1Mo-0.8Ta-Y and Ti-6Al-4V-Y Alloys

Small amounts of yttrium additions to Ti-6Al-2Nb-1Mo-0.8Ta and Ti-6Al-4V decrease the flow stress and increase the superplastic forming rates. The superplasticity improvements result from reduced interstitial oxygen as the result of scavenging of oxygen by yttrium and grain-growth retardation by Y dispersoids.

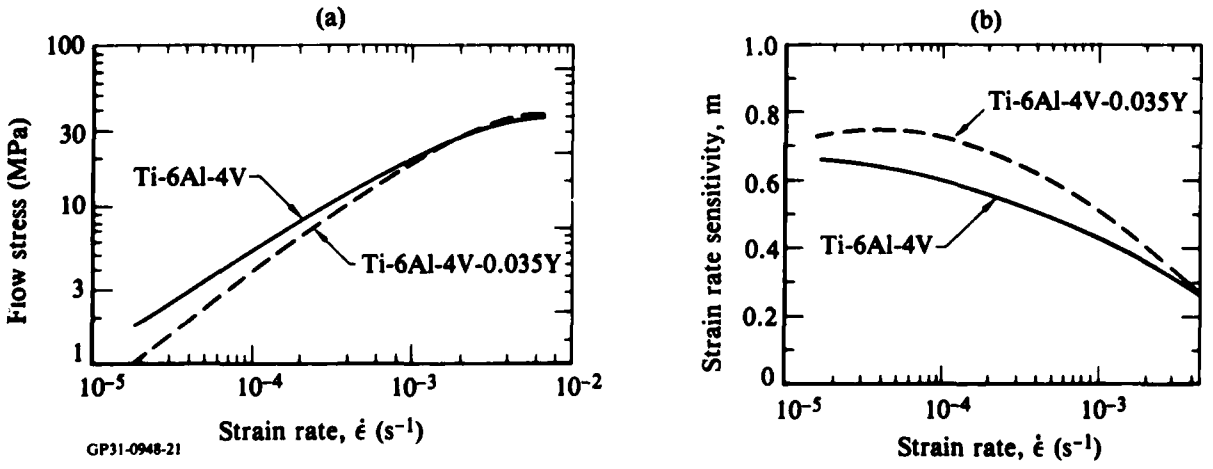

Figure 22. Effect of yttrium addition on (a) flow stress and (b) strain sensitivity of Ti-6Al-4V at 906°C.

4. INFLUENCE OF YTTRIUM ADDITIVES ON THE WELDABILITY OF Ti-6Al-2Nb-1Mo-0.8Ta

4.1 Beneficial Effects of Yttrium Additives on the Weldability of Ti Alloys

The presence of Er and Y dispersoids in Ti effect significant microstructural refinement and retard grain-growth at elevated temperatures. Welding is an important fabrication technique, which would receive even wider application to Ti alloys were it not for the resulting grain-growth and consequent loss of strength which accompany the welding process. Simpson (Reference 18) reported that Y in the weld filler-metal reduces the weld-zone grain size by a factor of 20 in Ti-6Al-6V-2Sn, but Chasteen et al. (Reference 19) claimed that 0.025 wt% Y degraded the weld strength of Ti-5Al-5Sn-2Mo-2Zr-0.25Si. Hayes et al. (Reference 20) used rare-earth additives to control hydrogen embrittlement of welded HY-130 steel.

Because of their high-temperature reactivity, Ti alloys are usually welded either in a vacuum chamber by electron-beam (EB) techniques or under an inert-gas shroud by the gas-tungsten-arc (GTA) method. EB welding is often limited by the vacuum chamber size, and GTA welding is inherently inferior because of large heat-affected zones and thermal distortions. Laser welding provides high-quality welds of small width/depth ratio with little thermal distortion and is not restricted by vacuum chamber size because vacuum is not required. Furthermore, operating conditions in laser welding are favorable for fast welding speeds and rapid solidification at the weld which permits joining materials with small mutual solid solubilities.

In the present investigation, Ti-6Al-2Nb-1Mo-0.8Ta specimens containing 0.01 and 0.025 wt% Y and 0.01 wt% Y_2O_3 were butt welded by laser welding and gas-tungsten-arc welding, and the effects of Y and Y_2O_3 additions on the mechanical properties of the weldments were determined.

4.2 Laser-Beam and Gas-Tungsten-Arc Welding of Ti-6211-Y Alloys

The alloys were prepared by the consumable-electrode, vacuum-arc-melting process followed by forging and hot rolling to ≈ 2 mm thicknesses. Butt welds without any filler material were made with the focused beam of a 1.5-kW CO_2 laser using the experimental arrangement shown in Figure 23a. The laser beam was fixed, and the specimens to be welded were traversed at controlled rates

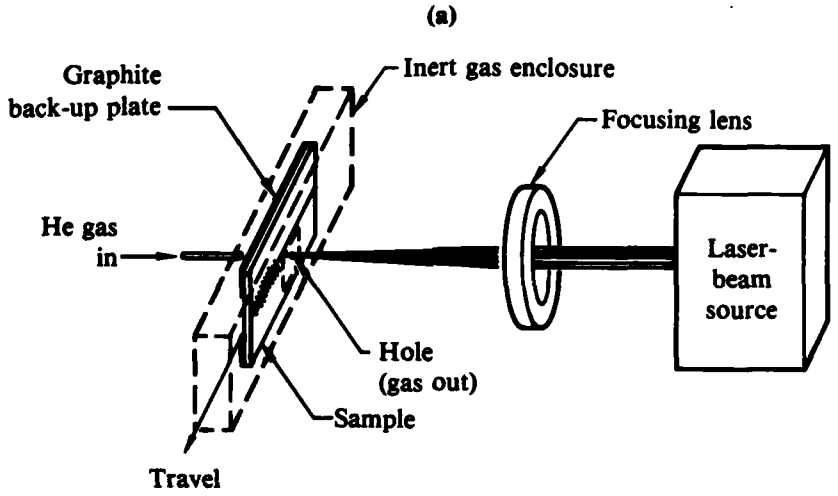

Figure 23. Schematic diagram of the experimental arrangements for (a) laser welding and (b) gas-tungsten-arc welding of Ti-6Al-2Nb-1Mo-0.8Ta-Y alloys.

in a plane perpendicular to the laser beam. A graphite plate was placed behind the alloy sheets to prevent burn-through of the support fixture by the laser beam. A gas shroud of flowing He covered the specimen area where the laser beam was focused. Bead-on-plate melts were produced to determine the process parameters for full-penetration welds.

Gas-tungsten-arc welds were produced using a copper back-up plate fixture with an Ar gas shroud around the electrode and weldment (Figure 23b). Argon gas under pressure flows coaxially around the electrode and from a side tube toward the weldment in a semi-enclosure. Argon also flows under the sample to provide an inert gas atmosphere at the back of the weldment. The process parameters for gas-tungsten-arc and laser weldings used in this investigation are listed in Tables 2 and 3.

4.3 Tensile Properties of Ti-6211-Y Weldments

The room-temperature tensile properties of transverse-oriented laser-beam and GTA welded Ti-6211-Y alloys are summarized in Tables 4 and 5. The alloy containing 0.025 Y has the best combination of strength and ductility. The differences in the ductilities of laser-welded and GTA-welded specimens are probably caused by differences in interstitial pick-up during welding.

The principal conclusion of this study is that small Y additions to Ti-6Al-2Nb-1Mo-0.8Ta weldments result in ~ 30-40% increase in ductility without adversely affecting strength.

TABLE 2. OPERATING PARAMETERS FOR LASER WELDING OF Ti-6Al-2Nb-1Mo-0.8Ta-Y ALLOYS.

Specimen thickness (cm)	0.2
Laser system	1.5 kW, CO_2, continuous wave at 10.6-μm wavelength
Fixturing	Graphite backing and hold-down tabs
Shield gas	He at pressures of 136 kPa flows around the sample in an enclosure
Beam power, incident (W)	700, 810
Beam focus, spot diameter (mm)	1
Beam scanning rate (cm/s)	0.25

GP31-0948-27

TABLE 3. OPERATING PARAMETERS FOR GAS-TUNGSTEN-ARC WELDING OF Ti-6Al-2Nb-1Mo-0.8Ta-Y ALLOYS.

Specimen thickness (cm)	0.2
Fixturing	Copper backing and hold-down tabs
Electrode	~ 3 mm diam, 2% thoriated tungsten with 60° conical tip
Shield gas	Ar at 197 cm^3/s, trailing shield and back purge provided.
Arc voltage (V)	9.8
Welding current (A)	190
Electrode travel rate (cm/s)	0.17

GP31-0948-26

TABLE 4. ULTIMATE TENSILE STRENGTHS OF LASER-WELDED AND GTA-WELDED Ti-6211-Y ALLOYS.

Alloy	Ultimate tensile strength [MPa]	
	Laser-welded specimens	GTA-welded specimens
Ti-6Al-2Nb-1Mo-0.8Ta	780	938
Ti-6Al-2Nb-1Mo-0.8Ta-0.01Y	887	973
Ti-6Al-2Nb-1Mo-0.8Ta-0.025Y	938	945
Ti-6Al-2Nb-1Mo-0.8Ta-0.01Y_2O_3	904	910

GP31-0948-30

TABLE 5. DUCTILITIES OF LASER-WELDED Ti-6Al-2Nb-1Mo-0.8Ta-Y ALLOYS.

Alloy	Total elongation (%)	
	Laser-welded specimens	GTA-welded specimens
Ti-6Al-2Nb-1Mo-0.8Ta	5.4	8.7
Ti-6Al-2Nb-1Mo-0.8Ta-0.01Y	5.0	10.5
Ti-6Al-2Nb-1Mo-0.8Ta-0.025Y	7.5	10.9
Ti-6Al-2Nb-1Mo-0.8Ta-0.01Y_2O_3	6.6	7.8

GP31-0011-28

5. SUPERPOSITION OF STRENGTHENING MECHANISMS IN Ti-Al-Si AND Ti-Al-Y ALLOYS

5.1 Strengthening of $Ti_3Al(\alpha_2)$ Precipitation-Strengthened Ti-Al Alloys

In titanium-aluminum alloys with aluminum concentrations between 10 and 20 at.%, the ordered and coherent α_2 phase (based on the composition Ti_3Al and having an ordered DO_{19} lattice structure) is precipitated upon aging. Precipitation strengthening in these alloys is generally accompanied by a significant loss of ductility, which has been attributed to the formation of coarse planar-slip bands leading to stress concentrations at grain boundaries and slip-band intersections in the early stages of deformation. Plastic deformation in this type of alloy occurs by the shearing of α_2 precipitates by glide dislocations.

The strength and ductility of Ti_3Al precipitation-strengthened Ti-Al alloys are related to the grain size, concentration of aluminum, volume fraction of Ti_3Al precipitates, and interstitial oxygen concentration (References 14, 21-23). Although the individual effects of microstructural variables on tensile properties have been investigated, the strengthening resulting from combinations of different microstructural variables has not received attention. The present investigation was conducted with the objective of determining the combined effects on strength and ductility of interstitial oxygen, grain size, coherent Ti_3Al precipitates, and incoherent dispersoids.

The Ti-Al-Si and Ti-Al-Y alloys are particularly suited for a study of the superposition of strengthening mechanisms because slip barriers of widely differing strengths can be produced by the proper choice of alloying element concentrations and heat treatments. By varying the Al concentration from 5 to 10 wt% and annealing the alloys at 500-1100°C, different combinations of substitutional solid solutions, coherent Ti_3Al, and incoherent Ti_3Al precipitates with volume fractions of 0.2-0.6 were produced. The grain size of the alloys was varied by hot rolling at 600°C followed by annealing at 800-900°C. Additional solid-solution strengthening and dispersion strengthening were produced by Si and Y additions.

5.2 Preparation and Processing of Ti-Al-Si and Ti-Al-Y Alloys

0.25 kg button ingots of the alloy compositions shown in Table 6 were prepared by vacuum arc melting the alloys in a water-chilled copper hearth. Each button was prepared from a mixture of Ti-50A grade titanium, high-purity aluminum, and 99.9% pure yttrium and silicon. The button ingots were hot rolled to 3.5 mm sheets. The Ti-8.5Al-1.0Y, Ti-8.5Al-2.0Y, and Ti-8.5Al-2.5Si alloys cracked severely during rolling and could not be rolled to 3.5 mm sheets.

The hot-rolled alloys were annealed at 800-930°C to produce variations in grain sizes and at 550-750°C to produce Ti_3Al (α_2) precipitates.

5.3 Tensile Properties of Ti-Al-Y and Ti-Al-Si Alloys

The room-temperature tensile properties of Ti-Al, Ti-Al-Y, and Ti-Al-Si alloys with different combinations of grain size and α_2 precipitate density are listed in Tables 7-9. The Ti-8.5Al, Ti-10.0Al, Ti-8.5Al-0.5Y, Ti-8.5Al-0.2Si, Ti-8.5Al-0.5Si, and Ti-8.5Al-1.0Si alloys aged at 550-750°C fractured before the onset of plastic deformation, and yield stresses of these alloys could not be determined.

TABLE 6. NOMINAL COMPOSITIONS OF ALLOYS USED FOR STUDIES ON SUPERPOSITION OF STRENGTHENING MECHANISMS IN Ti-Al-Si AND Ti-Al-Y ALLOYS.

Ti-4.0Al
Ti-5.5Al
Ti-7.0Al
Ti-8.5 Al
Ti-10.0 Al
Ti-8.5Al-0.5Y
Ti-8.5Al-1.0Y
Ti-8.5Al-2.0Y
Ti-8.5Al-0.2Si
Ti-8.5Al-0.5Si
Ti-8.5Al-1.0Si
Ti-8.5Al-2.5Si

GP31-0948-24

TABLE 7. GRAIN SIZES AND YIELD STRESSES OF Ti-4.0Al, Ti-5.5Al, AND Ti-7.0Al ALLOYS ANNEALED AT 550-800°C.

Heat treatment	Ti-4.0Al		Ti-5.5Al-0.5Y		Ti-7.0Al	
	Grain size (μm)	Yield stress (MPa)	Grain size (μm)	Yield stress (MPa)	Grain size (μm)	Yield stress (MPa)
800°C/30 min, water quenched (WQ)	28	519	22	647	24	730
800°C/30 min, WQ +550°C/100 h	25	544	26	674	25	804
800°C/30 min, WQ +650°C/100 h	28	547	28	662	30	773
800°C/30 min, WQ +750°C/100 h	28	517	25	657	24	738
850°C/120 min, WQ	38	533	38	651	43	718
850°C/120 min, WQ +550°C/100 h	28	501	25	654	35	723
850°C/120 min, WQ +650°C/100 h	42	549	32	674	46	722
850°C/120 min, WQ +750°C/100 h	35	520	36	672	45	723
850°C/18 h, WQ	82	515	70	625	63	642
850°C/18 h, WQ +550°C/100 h	65	535	50	674	48	678
850°C/18 h, WQ +650°C/100 h	76	509	54	651	53	709
850°C/18 h, WQ +750°C/100 h	54	521	56	640	89	669

GP31-0948-33

TABLE 8. GRAIN SIZES AND YIELD STRESSES OF Ti-8.5Al, Ti-8.5Al-0.5Y, AND Ti-10.0Al ALLOYS ANNEALED AT 930°C.

Heat treatment	Ti-8.5Al		Ti-8.5Al-0.5Y		Ti-10.0Al	
	Grain size (μm)	Yield stress (MPa)	Grain size (μm)	Yield stress (MPa)	Grain size (μm)	Yield stress (MPa)
930°C/10 min, water quenched	33	769	19	767	28	770
930°C/120 min, water quenched	41	738	23	772	38	758
930°C/18 h, water quenched	78	714	29	762	86	769

GP31-0948-32

TABLE 9. GRAIN SIZES AND YIELD STRESSES OF Ti-8.5Al-0.2Si, Ti-8.5Al-0.5Si, AND Ti-8.5Al-1.0Si ALLOYS ANNEALED AT 930°C AND WATER QUENCHED TO 25°C.

Heat treatment	Ti-8.5Al-0.2Si		Ti-8.5Al-0.5Si		Ti-8.5Al-1.0Si	
	Grain size (μm)	Yield stress (MPa)	Grain size (μm)	Yield stress (MPa)	Grain size (μm)	Yield stress (MPa)
930°C/120 min, water quenched	37	856	46	835	19	960
930°C/18 h, water quenched	82	746	77	762	28	890

GP31-0948-34

5.4 Grain-Size Strengthening in Ti-Al Alloys

Figures 24a-24d show the variations in 0.2% yield stress ($\sigma_{0.2}$) with the reciprocal of the grain size for differently heat-treated Ti-Al alloys. The data can be reasonably represented by straight lines. The linear variation of $\sigma_{0.2}$ with $d^{-1/2}$ for the aged and unaged alloys indicates that the 0.2% flow stress obeys the Hall-Petch relation. In the solution-treated condition, the Hall-Petch slope is higher in Ti-7.0Al and Ti-8.5Al alloys than in the other alloys. Upon aging the alloys at 550 and 650°C, the Hall-Petch slope is unaltered in Ti-4.0Al and Ti-5.5Al alloys and is significantly increased in Ti-7.0Al alloy. The Hall-Petch slope of aged Ti-8.5Al and Ti-10.0Al alloys could not be determined because of pre-yield fracture. The increased Hall-Petch slope in the aged Ti-7.0Al alloy is attributed to the effect on slip transmittal of the shearable coherent Ti_3Al precipitates.

5.5 Solid-Solution Strengthening in Ti-Al Alloys

The dependence of 0.2% yield stress on aluminum concentration, c, is shown as a plot of $\sigma_{0.2}$ vs $c^{1/2}$ in Figure 25. In the solution-treated condition, the $\sigma_{0.2}$ vs $c^{1/2}$ plot is linear up to ~ 8.5 wt% Al in accordance with the predicted behavior of dilute solid solutions (Reference 24). The deviations from linearity at higher aluminum concentrations are caused by the presence of short-range ordered regions and fine Ti_3Al precipitates in the as-quenched alloys. In the alloys aged at 550°C, the slope of $\sigma_{0.2}$ vs $c^{1/2}$ is significantly increased because of the formation of coherent Ti_3Al precipitates.

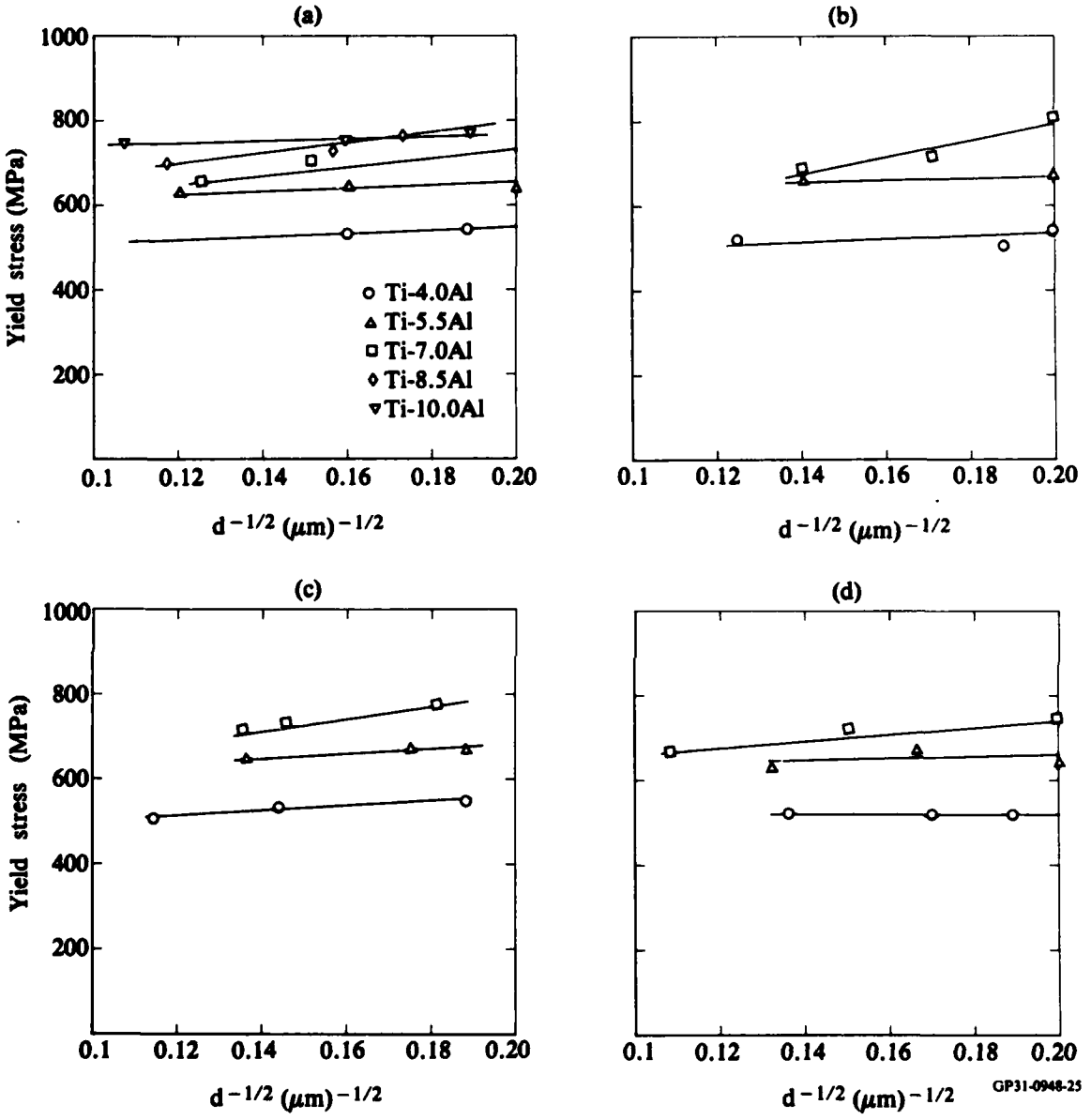

Figure 24. Grain-size dependence of yield stress in Ti-Al alloys (a) solution treated, (b) aged at 550°C for 100 h, (c) aged at 650°C for 4 h, and (d) aged at 750°C for 1 h.

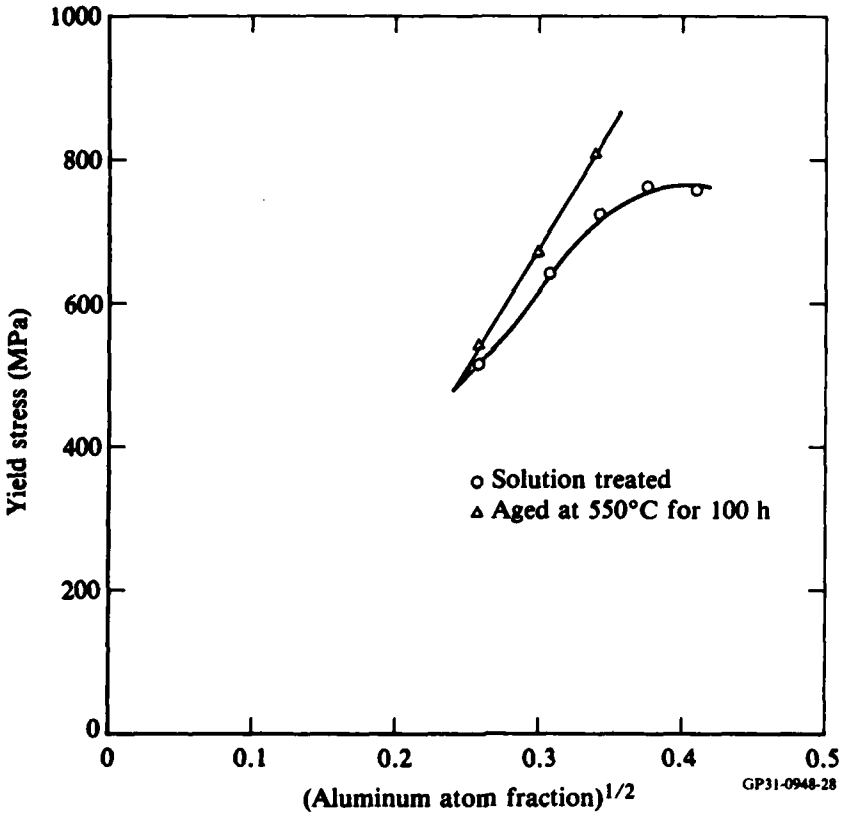

Figure 25. Influence of aluminum concentration on the yield stress of solution-treated-and-aged Ti-Al alloys (grain size = 25 μm).

5.6 Effects of Y Additions on the Yield Stress of Ti-8.5Al

The yield stress as a function of $d^{-1/2}$ for Ti-8.5Al and Ti-8.5Ai-0.5Y alloys is plotted in Figure 26. At identical grain sizes, the yield stresses of Ti-8.5Al-0.5Y alloys are lower than that of Ti-8.5Al alloys. This effect can be explained only if oxygen scavenging by yttrium is assumed so that dispersion strengthening by Y is offset by this reduction in flow stress. The weak grain size dependence of yield stress in Ti-8.5Al-0.5Y is in accordance with previous observations of grain size effects in dispersion strengthened titanium alloys (Reference 25). In the presence of dispersoids, the initial mean slip length is the interparticle spacing, not the grain size, and therefore the 0.2% yield stress is dependent more on interparticle spacing than on grain size in the dispersion-containing alloys.

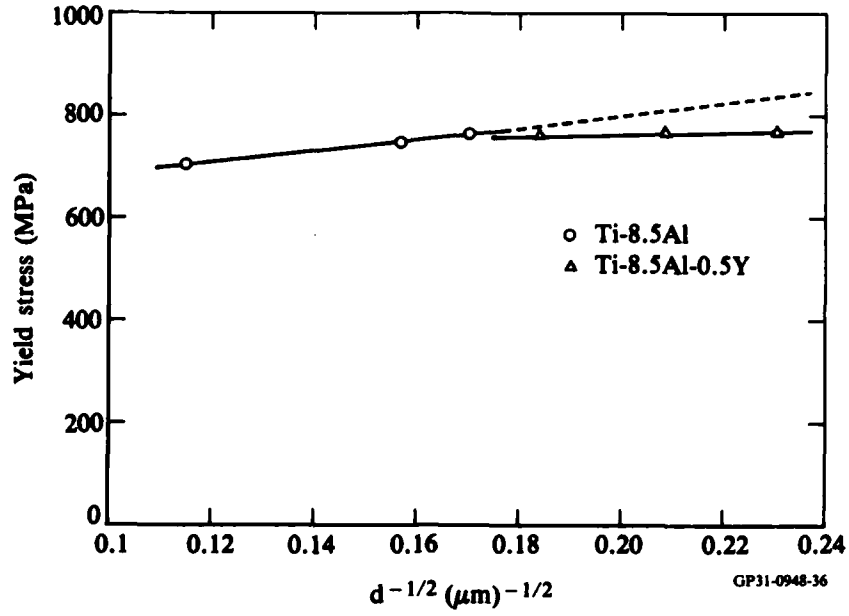

Figure 26. Grain-size dependence of yield stress in Ti-8.5Al and Ti-8.5Al-0.5Y alloys.

5.7 Effects of Si Additions on the Yield Stress of Ti-8.5Al

The grain-size dependences of yield stresses in Ti-8.5Al and Ti-8.5Al-Si alloys are shown in Figure 27. The Hall-Petch slope is higher in silicon containing alloys than in Ti-8.5Al. A single linear relation between yield stress and $d^{-1/2}$ for different silicon concentrations indicates that the strength increments in Ti-8.5Al-Si alloys are caused predominantly by the grain refinement effected by silicon. The effect of silicon on friction stress of Ti-8.5Al alloy is negligible. This result is important because previously it had been assumed that the strength increments produced by different solute elements in Ti are additive (Reference 26). The results of the present investigation clearly show that when the grain-size differences are taken into account, the rule of additivity does not hold for strengthening by different solute elements. The higher Hall-Petch slope in silicon-containing alloys results from the strengthening of grain boundaries by silicon.

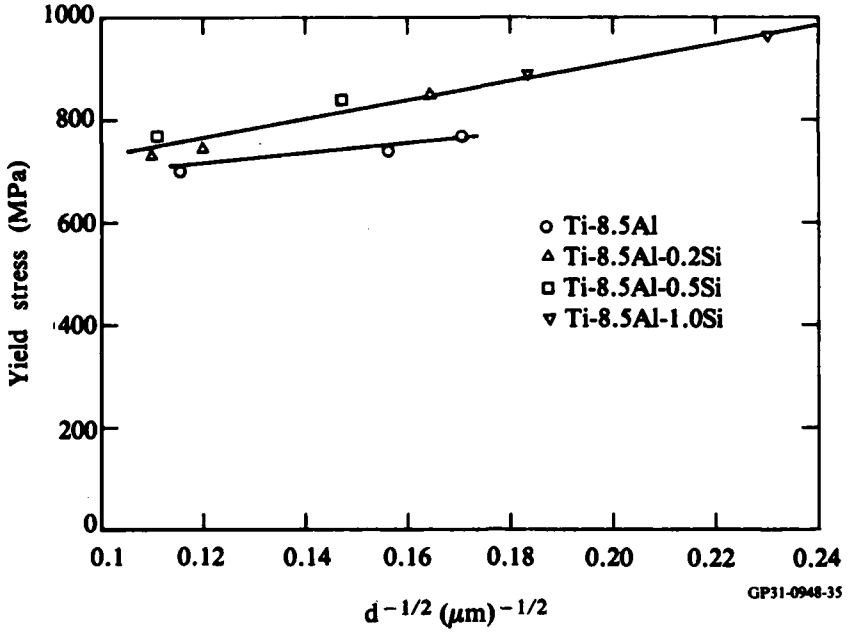

Figure 27. Grain-size dependence of yield stress in Ti-8.5Al and Ti-8.5Al-Si alloys.

5.8 Summary of Superposition of Strengthening Mechanisms in Ti-Al-Si and Ti-Al-Y Alloys

The superposition of solid-solution strengthening, precipitation strengthening, and grain-size strengthening in ingot-processed Ti-xAl (x = 4, 5.5, 7.0, 8.5, and 10.0), Ti-8.5Al-0.5Y, and Ti-8.5Al-ySi (y = 0.2, 0.5, and 1.0) alloys was studied. The Hall-Petch slope decreased with decreasing Al concentration, decreasing coherent Ti_3Al, and increasing incoherent dispersoids. The expected dispersion strengthening in Ti-8.5Al-0.5Y alloys was not observed because of the scavenging of interstitial oxygen by Y and large (> 1 μm) interparticle spacings of Y-containing dispersoids. Silicon additions to Ti-8.5Al produced strength increments of 50-140 MPa. These strength increments resulted mainly from the grain refinement by Si and the increased Hall-Petch slope in silicon-containing alloys.

6. CONCLUSIONS

1. Rapid solidification at cooling rates > 10^4 K/s results in homogeneously distributed, closely spaced, 10-100 nm, incoherent dispersoids in Ti-8Al-1.0Y, Ti-8Al-2.0Y, and Ti-8Al-1.5Er alloys. The incoherent dispersoids produce 30-60% strength increments and are conducive to dispersing planar slip in Ti/high-Al alloys.

2. Small yttrium additions to Ti-6Al-2Nb-1Mo-0.8Ta and Ti-6Al-4V decrease the high-temperature flow stress and increase the superplastic forming rates.

3. Small Y additions to Ti-6Al-2Nb-1Mo-0.8Ta weldments results in 30-40% increase in ductility without adverse effects on strength.

4. The Hall-Petch slope of Ti-Al alloys decreases with decreasing Al concentration, decreasing coherent Ti_3Al, and increasing incoherent dispersoids.

5. Yttrium additions to ingot-processed Ti/high-Al alloys do not produce additional strengthening because of scavenging of interstitial oxygen by yttrium and large interparticle spacings.

6. 0.2-1.0 wt% silicon additions to Ti-8.5Al produce strength increments of 50-140 MPa. The strength increments result mainly from the grain refinement by Si and the increased Hall-Petch slope in silicon-containing alloys.

REFERENCES

1. C. R. Whitsett, S. M. L. Sastry, J. E. O'Neal, and R. J. Lederich, Influence of Rare-Earth Additions on Properties of Titanium Alloys: Microstructures and Room-Temperature Tensile Properties of Ti-6Al-4V with Yttrium, Erbium, and Mischmetal Additions, McDonnell Douglas Report MDC Q0627 (31 May 1977), Technical Report, ONR Contract No. N00014-76-C-0626.

2. C. R. Whitsett, S. M. L. Sastry, J. E. O'Neal, and R. J. Lederich, Influence of Rare-Earth Additions on Properties of Titanium Alloys: Room-Temperature Tensile Properties and Fracture Toughness of Ti-6Al-4V with Erbium, Yttrium, and Yttria Additions, McDonnell Douglas Report MDC Q0654 (31 May 1978), Technical Report, ONR Contract No. N00014-76-C-0626.

3. S. M. L. Sastry, R. J. Lederich, P. S. Pao, and J. E. O'Neal, Influence of Rare-Earth Additions on Properties of Titanium Alloys: Plane-Strain Fracture Toughness, Creep, and High-Temperature Deformation of Ti-6Al-4V with Erbium and Yttrium Additions, McDonnell Douglas Report MDC Q0684 (31 May 1979), Technical Report, ONR Contract No. N00014-76-C-0626.

4. S. M. L. Sastry, R. J. Lederich, P. S. Pao, and J. E. O'Neal, Influence of Rare-Earth Additions on Properties of Titanium Alloys: Effects of Yttrium and Erbium Additives on Ti-8Al and Ti-10Al Alloys, McDonnell Douglas Report MDC Q0718 (31 August 1980), Technical Report, ONR Contract No. N00014-76-C-0626.

5. S. M. L. Sastry, R. J. Lederich, P. S. Pao, and J. E. O'Neal, Influence of Rare-Earth Additions on Properties of Titanium Alloys: High-Temperature Deformation, Room-Temperature Fracture Toughness, and Fatigue Crack-Growth of Ti-6Al-2Nb-1Ta-0.8Mo with Yttrium and Yttria Additions, McDonnell Douglas Report Q0728 (31 August 1980), Technical Report, ONR Contract No. N00014-76-C-0626.

6. H. E. Cline and T. R. Anthony, Heat Treating and Melting Material with a Scanning Laser or Electron Beam, J. Appl. Phys. 48, 3895 (1977).

7. T. C. Peng, S. M. L. Sastry, and J. E. O'Neal, Exploratory Study of Laser Processing of Titanium Alloys, Lasers in Metallurgy Symposium, 110th AIME Annual Meeting, Chicago, IL, 22-26 February 1981.

8. T. C. Peng, S. M. L. Sastry, and J. E. O'Neal, A Correlation Between Dendrite-Arm-Spacing and Cooling Rate for Laser-Melted Ti-15V-3Al-3Sn-3Cr, International Conf. on Applications of Lasers in Materials Processing, Los Angeles, CA, 24-26 January 1983.

9. O. Esquivel, J. Maxumder, M. Bass, and S. Copley, Shape and Surface Relief of Continuous Laser-Melted Trails in UDIMET 700, In **Rapid Solidification Processing: Principles and Technologies, II** (Claitor's Publ. Div., Baton Rouge, LA, 1980), p. 180.

10. P. R. Strutt, M. Kurup, and D. A. Gilbert, Comparative Study of Electron Beam and Laser Melting of M2 Tool Sheet, In **Rapid Solidification Processing: Principles and Technologies, V** (Claitor's Publ. Div., Baton Rouge, LA, 1980), p. 225.

11. R. P. Elliott, **Constitution of Binary Alloys, First Supplement** (McGraw Hill Publishing Company, New York, NY, 1965) p. 407, 854.

12. M. F. Ashby, On the Orowan Stress, In **Physics of Strength and Plasticity**, ed. by A. S. Argon (M.I.T. Press, Cambridge, MA, 1969), p. 113.

13. P. B. Hirsch and J. F. Humphreys, Plastic Deformation of Two-Phase Alloys Containing Small Nondeformable Particles, In **Physics of Strength and Plasticity**, ed. by A. S. Argon (M.I.T. Press, Cambridge, MA, 1969), p. 189.

14. M. G. Mendiratta, S. M. L. Sastry, and J. V. Smith, Effect of Grain Size Upon Flow and Fracture in a Precipitation-Strengthened Ti-8w/oAl-0.25w/oSi Alloy, J. Mat. Sci. 11, 1835 (1976).

15. J. K. Tien, Alloy Design with Oxide Dispersions and Precipitates, In **Fundamental Aspects of Structural Alloy Design**, ed. by R. I. Jaffee and B. A. Wilcox (Plenum Press, New York, NY, 1977), p. 363.

16. S. M. L. Sastry, R. J. Lederich, T. L. Mackay, and W. R. Kerr, Superplastic Forming Characterization of Titanium Alloys, J. Metals **35**, 48, (1983).

17. R. J. Lederich, S. M. L. Sastry, T. L. Mackay, and M. Hayase, Superplastic Formability Testing, J. Metals **34**, 16 (1982).

18. R. P. Simpson, Controlled Weld-Pool Solidification Structure and Resultant Properties with Yttrium Inocculation of Ti-6Al-6V-2Sn Welds, Welding J., Research Supplement **56**, 67s (1977).

19. J. W. Chasteen and M. H. Horowitz, Some Effects of Yttrium on Ti-5522S Alloy Weld, Welding J., Research Supplement **57**, 196s (1978).

20. M. D. Hayes and D. Hauser, Hydrogen in HY-130 Weld Metal, Battelle Columbus Labs. Report NR031-770 (14 May 1979), Final Report, ONR Contract No. N00014-74-C-0407.

21. J. C. Williams and M. J. Blackburn, The Structure, Mechanical Properties and Deformation Behavior of Ti-Al and Ti-Al-X Alloys, In **Ordered Alloys: Structural Applications and Physical Metallurgy**, ed. by B. H. Kear, C. T. Sims, N. S. Stoloff, and J. H. Westbrook (Claitor's Publ. Div., Baton Rouge, LA, 1970), p. 425.

22. G. Lütjering and S. Weissman, Mechanical Properties of Age Hardened Titanium-Aluminum Alloys, Acta Met. **18**, 785 (1970).

23. M. G. Mendiratta, Tensile Properties to 650°C and Deformation Structures in a Precipitation-Strengthened Titanium-Aluminum Alloy, NASA Technical Note TN D-7325 (June 1973).

24. P. Haasen, Mechanical Properties of Solid Solutions and Intermetallic Compounds, In **Physical Metallurgy**, ed. by R. W. Cahn (North-Holland Publishing Company, Amsterdam, 1970), p. 1011.

25. S. M. L. Sastry, J. E. O'Neal, R. J. Lederich, and B. B. Rath, The Effects of Yttrium and Erbium Dispersoids on the Deformation Behavior of Titanium, J. Matl. Sci. **14**, p. 183 (1979).

26. H. Conrad, M. Dhoner, and B. de Meester, Deformation and Fracture - Critical Review, In **Titanium Science and Technology**, ed. by R. I. Jaffee and H. M. Burte (Plenum Press, New York, 1973), p. 969.

	Copies
Naval Sea System Command Washington, D.C. 20362 Attn: Code 035	1
Naval Facilities Engineering Command Alexandria, VA 22331 Attn: Code 03	1
Scientific Advisor Commandant of the Marine Corps Washington, D.C. 20380 Attn: Code AX	1
Naval Ship Engineering Center Department of the Navy Washington, D.C. 20360 Attn: Code 6101	1
Army Research Office P.O. Box 12211 Triangle Park, NC 27709 Attn: Metallurgy & Ceramics Program	1
Army Materials and Mechanics Research Center Watertown, MA 02172 Attn: Research Programs Office	1
Air Force Office of Scientific Research Bldg. 410 Bolling Air Force Base Washington, D.C. 20332 Attn: Chemical Science Directorate	1
Electronics & Solid State Sciences Directorate	1
Air Force Materials Laboratory Wright-Patterson AFB Dayton, OH 45433	1
Library Building 50, Rm 134 Lawrence Radiation Laboratory Berkeley, CA	1

	Copies
NASA Headquarters Washington, D.C. 20546 Attn: Code RRM	1
NASA Lewis Research Center 21000 Brookpark Road Cleveland, OH 44135 Attn: Library	1
National Bureau of Standards Washington, D.C. 20234 Attn: Metallurgy Division	1
Inorganic Materials Div.	1
Director Applied Physics Laboratory University of Washington 1013 Northeast Forthieth Street Seattle, WA 98105	1
Defense Metals and Ceramics Information Center Battelle Memorial Institute 505 King Avenue Columbus, OH 43201	1
Metals and Ceramics Division Oak Ridge National Laboratory P.O. Box X Oak Ridge, TN 37380	1
Los Alamos Scientific Laboratory P.O. Box 1663 Los Alamos, NM 87544 Attn: Report Librarian	1
Argonne National Laboratory Metallurgy Division P.O. Box 229 Lemont, IL 60439	1
Brookhaven National Laboratory Technical Information Division Upton, Long Island New York 11973 Attn: Research Library	1
Office Of Naval Research Branch Office 1030 East Green Street Pasadena, CA 91106	1

	Copies
Professor J. W. Morris, Jr. University of California College of Engineering Berkeley, CA 94720	1
Dr. Neil E. Paton Rockwell International Science Center 1049 Camino Dos Rios P.O. Box 1085 Thousand Oaks, CA 91360	1
Mr. A. Pollack Naval Ships R&D Center Code 2821 Annapolis, MD 21402	1
Professor W. F. Savage Rensselaer Polytechnic Institute School of Engineering Troy, New York 02181	1
Professor O. D. Sherby Stanford University Materials Sciences Division Stanford, CA 94300	1
Dr. G. Ecer Westinghouse Electric Corporation Research & Development Center Pittsburgh, PA 15235	1
Dr. E. A. Starke, Jr. Georgia Institute of Technology School of Chemical Engineering Atlanta, GA 30332	1
Professor David Turnbull Harvard University Division Engineering and Applied Physics Cambridge, MA 02138	1
Dr. F. E. Wawner University of Virginia School of Engineering and Applied Science Charlottesville, VA 22901	1
Dr. C. R. Whitsett McDonnell Douglas Research McDonnell Douglas Corporation Saint Louis, MO 63166	1
Dr. J. C. Williams Carnegie-Mellon University Department of Metallurgy and Materials Sciences Schenley Park Pittsburgh, PA 15213	1
Professor H. G. F. Wilsdorf University of Virginia School of Engineering and Applied Sciences Charlottesville, VA 22903	1
Professor R. Mehrabian University of Illinois at Urbana-Champaign 144 Mechanical Engineering Building Urbana, IL 61801	1
Dr. N. J. Grant Massachusetts Institute of Technology Department of Materials Science and Engineering Cambridge, MA 02139	1
Professor P. R. Strutt University of Connecticut School of Engineering Department of Metallurgy Storrs, CT 06268	1
Mr. I. Caplan David W. Taylor Naval Ship Research and Development Center Code 2813 Annapolis, MD 21402	1
Dr. G. R. Leverant Southwest Research Institute 3500 Culebra Road P.O. Box 28610 San Antonio, TX 78284	1

DISTRIBUTION

	Copies
Defense Documentation Center Cameron Station Alexandria, VA 22314	12
Office of Naval Research Department of the Navy 800 N. Quincy Street Arlington, VA 22217	
Attn: Code 471	1
Code 102	1
Code 470	1
Commanding Officer Office of Naval Research Branch Office Building 114, Section D 666 Summer Street Boston, MA 02210	1
Commanding Officer Office of Naval Research Branch Office 536 South Clark Street Chicago, IL 60605	1
Office of Naval Research San Francisco Area Office One Hallidie Plaza Suite 601 San Francisco, CA 94102	1
Naval Research Laboratory Washington, D. C. 20375	
Attn: Code 6000	1
6100	1
6300	1
6400	1
2627	1
Naval Air Development Center Code 302 Warminster, PA 18964	
Attn: Mr. F. S. Williams	1
Naval Air Propulsion Test Center Trenton, NJ 08628	1
Attn: Library	1

	Copies
Naval Construction Batallion Civil Engineering Laboratory Port Hueneme, CA 93043	
Attn: Materials Division	1
Naval Electronics Laboratory San Diego, CA 92152	
Attn: Electron Materials Sciences Division	1
Naval Missile Center Materials Consultant Code 3312-1 Point Mugu, CA 92041	1
Commanding Officer Naval Surface Weapons Center White Oak Laboratory Silver Spring, MD 20910	
Attn: Library	1
David W. Taylor Naval Ship R&D Center Materials Department Annapolis, MD 21402	1
Naval Undersea Center San Diego, CA 92132	
Attn: Library	1
Naval Underwater System Center Newport, RI 02840	
Attn: Library	1
Naval Weapons Center China Lake, CA 93555	
Attn: Library	1
Naval Postgraduate School Monterey, CA 93940	
Attn: Mechanical Engineering Department	1
Naval Air Systems Command Washington, D.C. 20360	
Attn: Code 52031	1
52032	1

	Copies
Professor G. S. Ansell Rensselaer Polytechnic Institute Dept. of Metallurgical Engineering Troy, NY 02181	1
Professor H. K. Birnbaum University of Illinois Department of Metallurgy Urbana, IL 61801	1
Dr. E. M. Breinan United Technology Corporation United Technology Research Laboratories East Hartford, CT 06108	1
Professor H. D. Brody University of Pittsburgh School of Engineering Pittsburgh, PA 15213	1
Mr. R. Morante General Dynamics Electric Boat Division Eastern Point Road Groton, CT 06340	1
Professor J. B. Cohen Northwestern University Dept. of Material Sciences Evanston, IL 60201	1
Professor M. Cohen Massachusetts Institute of Technology Department of Metallurgy Cambridge, MA 02139	1
Professor Thomas W. Eager Massachusetts Institute of Technology Department of Materials Science and Engineering Cambridge, MA 02139	1
Professor B. C. Giessen Northeastern University Department of Chemistry Boston, MA 02115	1
Professor D. G. Howden Ohio State University Dept. of Welding Engineering 190 West 19th Avenue Columbus, OH 43210	1
Dr. C. S. Kortovich Dr. C. S. Kortovich TRW, Inc. 23555 Euclid Avenue Cleveland, OH 44117	1
Professor D. A. Koss Michigan Technological University College of Metallurgical Engineering Houghton, MI 49931	1
Professor A. Lawley Drexel University Dept. of Metallurgical Engineering Philadelphia, PA 19104	1
Professor Harris Marcus The University of Texas at Austin College of Engineering Austin, TX 78712	1
Dr. H. Margolin Polytechnic Institute of New York 333 Jay Street Brooklyn, NY 11201	1
Professor K. Masubuchi Massachusetts Institute of Technology Department of Ocean Engineering Cambridge, MA 02139	1

END

FILMED

10-83

DTIC